Ocean Modelling 167 (2021) 101873

Contents lists available at ScienceDirect

Ocean Modelling

journal homepage: www.elsevier.com/locate/ocemod

Representing wave effects on currents

Leonel Romero [a,*], Delphine Hypolite [b], James C. McWilliams [b]

[a] Department of Marine Sciences, University of Connecticut, Groton, United States of America
[b] Department of Atmospheric and Oceanic Sciences and Institute of Geophysics and Planetary Physics, University of California, Los Angeles, United States of America

ARTICLE INFO

Keywords:
Wave–current interactions
Stokes drift
Wave breaking
Wave effects on currents

ABSTRACT

We describe a new framework to represent wave effects on currents, including several approximations (Stokes drift, Bernoulli head, and quasi-static pressure) and a parameterization of the vertical mixing due to wave breaking. The framework improves over existing methods not limited by water depth or monochromatic assumptions. The approximations are validated with spectra and current profiles from a model configuration in Southern California. The Stokes drift approximation uses two scales accounting for broadband spectra, including mixed wind-sea and swell. The Stokes drift is estimated iteratively, constrained by the surface drift velocity and Stokes transport, being more efficient while giving smaller errors compared to a spectrum reconstruction approach. One-month-long hydrostatic ocean model solutions at 270 m horizontal grid resolution show that waves have relatively small impacts on the mean circulation and mesoscale current variability near the surface. Waves increase the vorticity and divergence variance near the surface when the turbulent Langmuir number is small.

1. Introduction

Surface waves affect the upper-ocean circulation, air–sea fluxes, and cross-shelf exchange due to both conservative and non-conservative effects. Wave effects on currents (WEC) include wave-induced inertial oscillations (Hasselmann, 1970; McWilliams and Restrepo, 1999), Langmuir turbulence due to the Craik–Lebovich vortex force (Craik and Leibovich, 1976; McWilliams et al., 1997), enhanced near-surface mixing and modulation of the waterside stress due to wave-breaking (Agrawal et al., 1992; Terray et al., 1996; Craig and Banner, 1994; Sullivan et al., 2007; Janssen, 2012), non-breaking wave-induced vertical and horizontal mixing (Qiao et al., 2004; McWilliams et al., 2004; Herterich and Hasselmann, 1982; Weichman and Glazman, 2000), and material transport by the Stokes drift. Uchiyama et al. (2010) added WEC to the Regional Ocean Modeling System (ROMS) following the theoretical wave-average framework by McWilliams et al. (2004). The approach by Uchiyama et al. (2010), hereafter referred to as UMS10, is based on a WKB spectral peak approximation allowing for the coupling of ROMS with spectral wave models such as SWAN (Booij et al., 1999) or WAVEWATCHIII (The WAVEWATCH III Development Group [WW3DG], 2016). Kumar et al. (2013, 2015) applied the framework by UMS10 to study wave–current interactions across the inner-shelf and surf zone with regional model configurations of ROMS coupled to SWAN finding good performance against field observations.

WEC forcing should ideally be computed from directional wave spectra but is it not practical as it requires the exchange of large amounts of information between models especially for configurations with relatively large domains at high horizontal resolution. It is well known that the monochromatic approximation for deep-water waves results in an underestimation of the Stokes drift magnitude and shear near the surface compared to broadband computations (e.g., Kenyon, 1969; Rascle et al., 2006; Webb and Fox-Kemper, 2015; Lenain and Pizzo, 2020). To overcome this challenge several alternatives for coupled models have been proposed. Breivik et al. (2014) introduced a broadband approximation of the Stokes drift for deep-water waves and was recently updated to account for mixed wind-sea and swell (Breivik and Christensen, 2020). Kumar et al. (2017) proposed the use of a spectral reconstruction for coupled models based on the partitioning algorithm readily available in WAVEWATCHIII (Hanson and Phillips, 2001; Tracy et al., 2007; Hanson et al., 2009). In this study, we describe a set of wave approximations composed of Stokes drift, Bernoulli head, quasi-static pressure, and wave-induced vertical mixing due to unsteady non-breaking waves, and a parameterization of the vertical mixing to wave breaking suitable for coastal ocean models. The Stokes drift approximation builds on the work by Breivik et al. (2014) and Breivik and Christensen (2020) using an iterative two-scale approach that can handle mixed wind-sea and swell conditions and finite depth.

This manuscript is organized as follows: Section 2 describes the methods to represent WEC forcing and the model configuration. The framework is validated against direct computations from directional spectra of the regional model configuration, which is followed by a demonstration of ROMS solutions highlighting some of the impacts

* Corresponding author.
E-mail address: leonel.romero@uconn.edu (L. Romero).

https://doi.org/10.1016/j.ocemod.2021.101873
Received 25 January 2021; Received in revised form 30 July 2021; Accepted 10 August 2021
Available online 31 August 2021

due to WEC in Section 3. The results are summarized and discussed in Section 4.

2. Methods

The methods section first describes the governing equations of the ocean circulation and wave models which is followed by a description of the framework used to represent conservative and non-conservative WEC forcing, and the regional model configuration.

2.1. Governing equations

The governing equations of motion solved by a hydrostatic ROMS setup composed of the momentum, continuity, and tracers are

$$\frac{\partial \boldsymbol{u}}{\partial t} + \boldsymbol{u}\cdot\nabla_x\boldsymbol{u} + w\frac{\partial \boldsymbol{u}}{\partial z} + f\hat{\boldsymbol{z}}\times\boldsymbol{u} + \nabla_x p - \boldsymbol{F} - \frac{\partial}{\partial z}\left(K\frac{\partial \boldsymbol{u}}{\partial z}\right) = -\nabla_x\mathcal{K} + \boldsymbol{J} + \boldsymbol{F}^{\boldsymbol{w}} \tag{1}$$

$$\frac{\partial p}{\partial z} + \frac{g\rho}{\rho_o} = -\frac{\partial \mathcal{K}}{\partial z} + \boldsymbol{u}_s\cdot\frac{\partial \boldsymbol{u}}{\partial z} \tag{2}$$

$$\nabla_x\cdot\boldsymbol{u} + \frac{\partial w}{\partial t} = 0 \tag{3}$$

$$\frac{\partial c}{\partial t} + \boldsymbol{u}\cdot\nabla_x c + w\frac{\partial c}{\partial z} - F_c - \frac{\partial}{\partial z}\left(K_c\frac{\partial c}{\partial z}\right) = -\boldsymbol{u}_s\cdot\nabla_x c - w_s\frac{\partial c}{\partial z} + \frac{\partial}{\partial z}\left(K_{vw}\frac{\partial c}{\partial z}\right), \tag{4}$$

where the right hand side of (1), (2), and (4) correspond to WEC terms. The horizontal components of the current and derivative are $\boldsymbol{u}$ and ∇_x, respectively. The vertical velocity is w and vertical coordinate is z bounded between $-h \le z \le \eta + \hat{\eta}$, with $-h$ corresponding to the water depth, η is the ocean surface displacement from the mean ($z = 0$) and $\hat{\eta}$ is the quasi-static level component. The pressure is p, ρ is the density anomaly from the mean ρ_o, g is gravity, c represents the tracers (salinity and temperature), f is the Coriolis frequency, $\boldsymbol{F}$ and F_c are non-conservative forces, $\mathcal{K}$ is the Bernoulli head, $\boldsymbol{J} = -\hat{\boldsymbol{z}}\times\boldsymbol{u}_s[(\hat{\boldsymbol{z}}\cdot\nabla_x\times\boldsymbol{u}) + f] - w_s\frac{\partial \boldsymbol{u}}{\partial z}$ is the generalized vortex force, $\boldsymbol{F}^w$ represents wave-induced non-conservative forces, K_{vw} is the wave-induced tracer diffusivity, and the vertical eddy viscosity and diffusivity are K and K_c, respectively. Both K and K_c are modeled with the K-Profile Parameterization (KPP, Large et al., 1994) which can be enhanced to account for mixing due to wave breaking. The Stokes drift is non-divergent where horizontal components $\boldsymbol{u}_s$ are calculated from wave field and the vertical component $w_s(z) = -\nabla_x\cdot\int_{-h}^{z}\boldsymbol{u}_s(z')dz'$. The boundary conditions, including the usual tracer fluxes (not shown), are

$$\begin{aligned} K\frac{\partial}{\partial z}\boldsymbol{u}|_{\eta+\hat{\eta}} &= \frac{\tau_{oc}}{\rho_o} \\ K\frac{\partial}{\partial z}\boldsymbol{u}|_{-h} &= \frac{\tau_b}{\rho_o} \end{aligned} \tag{5}$$

with τ_{oc} and τ_b corresponding to the surface and bottom stresses, respectively, and

$$\begin{aligned} w|_{-h} &= -\boldsymbol{u}|_{-h}\cdot\nabla_x h \\ w|_{\eta+\hat{\eta}} &= \frac{\partial(\eta+\hat{\eta})}{\partial t} + (\boldsymbol{u}|_{\eta+\hat{\eta}}\cdot\nabla_x)(\eta+\hat{\eta}) + \nabla_x\cdot\boldsymbol{U}_s \end{aligned} \tag{6}$$

$$g\,\eta - p|_{\eta+\hat{\eta}} = \mathcal{P} \tag{7}$$

with the depth integrated Stokes drift $\boldsymbol{U}_s$ given by

$$\boldsymbol{U}_s = \int_{-h}^{\eta+\hat{\eta}}\boldsymbol{u}_s(z)dz. \tag{8}$$

The quasi-static level includes the wave induced set-down and inverse-barometric response to change in atmospheric pressure (here neglected). The right hand side term of (7) is the wave-induced higher-order quasi-static pressure. For more details on the numerical implementation refer to Uchiyama et al. (2010).

The wave field is modeled with WAVEWATCHIII, hereafter referred to as WW3, which solves the wave action conservation equation according to

$$\frac{\partial N(\boldsymbol{k})}{\partial t} + \frac{\partial}{\partial \boldsymbol{x}}\cdot\dot{\boldsymbol{x}}N(\boldsymbol{k}) + \frac{\partial}{\partial\theta}\dot{\theta}N(\boldsymbol{k}) + \frac{\partial}{\partial k}\dot{k}N(\boldsymbol{k}) = \frac{S_{in}+S_{nl}+S_{ds}+S_{bot}+S_{db}}{\sigma} \tag{9}$$

$$\dot{\boldsymbol{x}} = (\boldsymbol{c}_g + \boldsymbol{u}_{oc}) \tag{10}$$

$$\dot{\theta} = -\frac{1}{k}\frac{\partial\sigma}{\partial h}\frac{\partial h}{\partial m} - \boldsymbol{k}\cdot\frac{\partial \boldsymbol{u}_{oc}}{\partial m} \tag{11}$$

$$\dot{k} = -\frac{\partial\sigma}{\partial h}\frac{\partial h}{\partial s} - \boldsymbol{k}\cdot\frac{\partial \boldsymbol{u}_{oc}}{\partial s} \tag{12}$$

where $N(\boldsymbol{k}) = F(\boldsymbol{k})/\sigma(k)$ is the wave action, $F(\boldsymbol{k})$ is the directional wavenumber spectrum, $\sigma(k) = (gk\tanh kh)^{1/2}$ is the frequency according to the dispersion relationship, $\boldsymbol{c}_g = \partial\sigma/\partial\boldsymbol{k}$ is the group velocity, and $\boldsymbol{u}_{oc}$ is the surface current vector, s is a coordinate in the θ direction, and m is a coordinate perpendicular to s (Tolman and Booij, 1998). The source terms on the right side of Eq. (9) are the wind energy input S_{in}, nonlinear energy flux due to wave–wave resonant interactions S_{nl}, energy dissipation due to deep-water wave breaking S_{ds}, energy loss due to bottom friction S_{bot}, and energy dissipation due depth-induced breaking S_{db}. Although WW3 solves the wave action equation in wavenumber space, it can output the directional spectrum and source terms converted into the frequency domain (e.g., $\psi(f,\theta)$) at selected grid points. Currents effects on waves (CEW) are not accounted for in this study. The interested reader may refer to Romero et al. (2020) where CEW was analyzed in detail.

2.2. Wave approximations

Here we introduce a set of approximations of the Stokes drift, wave-induced vertical eddy diffusivity, Bernoulli head, and quasi-static pressure. This work is an effort to improve over existing methodologies, including the spectral peak monochromatic approach that is commonly used with coupled wave–ocean models (e.g., Uchiyama et al., 2010; Kumar et al., 2012, 2015). The approximations of this work are suitable for coastal models not limited to deep-water waves (e.g., Breivik et al., 2014; Breivik and Christensen, 2020).

The Stokes drift for a monochromatic wave is given by

$$\boldsymbol{u}_s(z) = \frac{A^2}{2}\sigma(k)\,\boldsymbol{k}\frac{\cosh 2k(z+h)}{\sinh^2 k\,D}, \tag{13}$$

where A is the wave amplitude, σ is the wave frequency which relates to the wavenumber k through the linear dispersion relationship $\sigma(k) = (gk\tanh kD)^{1/2}$, h is the water depth, and $D = h + \eta + \hat{\eta}$, with η corresponding to the surface elevation displacement, $\hat{\eta}$ is the wave induced set-down (Phillips, 1977; Uchiyama et al., 2010). In terms of the wave action A^2/σ, Eq. (13) becomes

$$\boldsymbol{u}_s(z) = g\frac{A^2}{\sigma(k)}k\,\boldsymbol{k}\frac{\cosh 2k(z+h)}{\sinh 2\,k\,D}, \tag{14}$$

which can be generalized for a wave directional frequency spectrum $\Psi(f,\theta)$ according to

$$\boldsymbol{u}_s(z) = 2g\iint\psi(f,\theta)\frac{k}{\sigma(k)}\boldsymbol{k}\frac{\cosh 2k(z+h)}{\sinh 2\,k\,D}df\,d\theta, \tag{15}$$

with $H_s = 4(\int\psi(f,\theta)\,df\,d\theta)^{1/2}$ corresponding to the significant wave height (Kenyon, 1969). The Stokes drift transport is obtained from (15) and (8) but because

$$\int_{-h}^{\eta+\hat{\eta}}\frac{\cosh 2k(z+h)}{\sinh 2\,k\,D}dz = \frac{1}{2k} \tag{16}$$

it becomes

$$\boldsymbol{U}_s = g\iint\psi(f,\theta)\frac{\boldsymbol{k}}{\sigma(k)}\,df\,d\theta. \tag{17}$$

Following Breivik et al. (2014), an effective wavenumber can be obtained from the ratio of the surface Stokes drift to the transport as given by

$$k_{se} = \frac{u_s(z=0)}{2U_s}. \tag{18}$$

This is based on the profile of a deep-water monochromatic wave by combining Eqs. (15)–(17).

We first approximate the Stokes drift according to

$$\boldsymbol{u}_{se} \approx \boldsymbol{u}_o \frac{\cosh 2k_{se}(z+h)}{\sinh 2k_{se}D}, \tag{19}$$

where $\boldsymbol{u}_o = \boldsymbol{u}_s(0)\tanh 2k_{se}D$ corresponds to a characteristic surface Stokes drift velocity. The approximation $\boldsymbol{u}_{se}$ is good near the surface for intermediate- and deep-water dominant waves. However, it decays much faster with depth than broadband calculations. In contrast, a monochromatic approximation of the form

$$\boldsymbol{u}_{sp}(z) \approx g\,\frac{A_w^2 k_p^2}{\sigma(k)}\frac{\cosh 2k_p(z+h)}{\sinh\,2k_p\,D}(\cos\overline{\theta}, \sin\overline{\theta}), \tag{20}$$

does a good job at depth and in shallow-water with the wave amplitude $A_w = \frac{H_s}{2\sqrt{2}}$, k_p being the peak wavenumber, and the spectrally weighted mean wave direction defined as

$$\overline{\theta} = \tan^{-1}\left(\frac{\iint \psi(f,\theta) f^{n_\theta}\sin\theta\, df d\theta}{\iint \psi(f,\theta) f^{n_\theta}\cos\theta\, df d\theta}\right). \tag{21}$$

The power $n_\theta = 0$ is commonly used.

In shallow-water ($k_p h < \pi/10$), the Stokes drift is approximated by

$$\boldsymbol{u}_{sa} \approx \boldsymbol{u}_{sp}, \tag{22}$$

and in deeper water, by combining $\boldsymbol{u}_{se}$ and $\boldsymbol{u}_{sp}$ with a switch function $H(z)$ according to

$$\boldsymbol{u}_{sa} \approx H(z)\boldsymbol{u}_{sp} + (1-H(z))\boldsymbol{u}_{se}. \tag{23}$$

The switch function

$$H(z) = \tanh\left(\frac{|z|k_{se}}{2}\right)^{1/2} \tag{24}$$

was found to work well over a wide range of conditions. Finally, $|\boldsymbol{u}_{sp}|$ is adjusted iteratively by minimizing the error of the Stokes drift transport to within less than 1%.

Following McWilliams et al. (2004), the vertical tracer square displacement and corresponding diffusivity for a monochromatic wave are given by

$$r_{vw}^2 = \left(A\frac{\sinh k(z+h)}{\sinh kD}\right)^2, \tag{25}$$

and

$$K_{vw} = \frac{1}{2}\left|\frac{\partial}{\partial t} r_{vw}^2\right|, \tag{26}$$

respectively, where the absolute value for the latter is introduced here to avoid negative diffusivities. The generalized vertical parcel displacement squared for a spectrum of waves gives

$$r_{vw}^2 = 2\iint \psi(f,\theta)\left(\frac{\sinh k(z+h)}{\sinh kD}\right)^2 df d\theta, \tag{27}$$

and the corresponding depth-integrated square displacement becomes

$$R_{vw}^2 = \int_{-h}^{\eta+\hat{\eta}} r_{vw}^2\, dz, \tag{28}$$

$$= \int 2\psi(f,\theta)\frac{\coth k\,D - k\,D\mathrm{csch}^2 k\,D}{2k}\, df d\theta. \tag{29}$$

In analogy to the Stokes drift approximation, the right-hand side of Eq. (29) is approximated by

$$R_{vw}^2 \approx \left(\frac{H_s}{2\sqrt{2}}\right)^2 \frac{\coth k_{re}\,D - k_{re}D\,\mathrm{csch}^2 k_{re}\,D}{2k_{re}}. \tag{30}$$

And the effective wavenumber k_{re} is first estimated from the r_{vw}^2 at the surface divided by the broadband value of R_{vw}^2

$$k_{re} = \frac{r_{vw}^2(z=0)}{2R_{vw}^2}. \tag{31}$$

Then it is corrected iteratively according to

$$k_{re} = \frac{r_{vw}^2(z=0)(\coth k_{re}\,D - k_{re}\,D\,\mathrm{csch}^2\,k_{re}\,D)}{2R_{vw}^2}. \tag{32}$$

starting with the initial guess to compute a new k_{re} and so on. The iteration converges after a few iterations (15 or less) and is not needed in deep-water ($k_p h > 2\pi$). Finally the vertical square particle displacement is approximated by

$$r_{vw}^2 \approx \left(\frac{H_s}{2\sqrt{2}}\frac{\sinh k_{re}(z+h)}{\sinh(k_{re}\,D)}\right)^2 \tag{33}$$

and the corresponding wave-induced vertical tracer diffusivity follows from Eq. (26). In the absence of R_{vw}^2 from a wave model, the particle displacement squared can be approximated alternatively using the mean wavelength

$$L_m = \int\int \frac{2\pi}{k}\frac{\psi(f,\theta)}{\langle\eta^2\rangle} df d\theta \tag{34}$$

with $k_{re} \approx 2\pi/L_m$ and r_{vw}^2 directly estimated from Eq. (33). Finally, if L_m is not available k_{re} can be approximated by k_p at the expense of significantly larger errors for r_{vw}^2 and K_{vw}.

The monochromatic wave-average quasi-static set-down according to Longuet-Higgins and Stewart (1962) is given by

$$\hat{\eta} = -\frac{A^2 k}{2\sinh 2kD}, \tag{35}$$

which for a wave spectrum becomes

$$\hat{\eta} = -\iint \frac{\psi(f,\theta)k}{\sinh 2\,k\,D}\, df d\theta. \tag{36}$$

The set-down for a broadband spectrum is generally smaller than a monochromatic approximation based on H_s and k_p for intermediate water depth. Assuming that $\hat{\eta}$ calculated spectrally is known, we calculate a filtered wave amplitude A_f such that a monochromatic approximation

$$\hat{\eta}_m \approx -\frac{A_f^2 k_p}{2\sinh 2\,k_p\,D}, \tag{37}$$

matches the broadband set-down at intermediate water depths or shallower ($k_p h < 2\pi$). Specifically,

$$A_f = A_w \min(1, (\hat{\eta}/\hat{\eta}_m)^{1/2}) \tag{38}$$

being limited to $A_f \le A_w$ since $\hat{\eta}_m$ becomes very small in deep water. The filtered wave amplitude A_f is used for the approximation of quasi-static pressure as described below.

The Bernoulli head without the quasi-static terms for a monochromatic wave is given by

$$\mathcal{K} = \frac{1}{4}\frac{\sigma A^2}{k\sinh^2 k\,D}\int_{-h}^{\eta+\hat{\eta}} \frac{\partial^2 \mathcal{V}}{\partial z^2}\sinh[2k(z'-z)]dz \tag{39}$$

where $\mathcal{V} = \boldsymbol{k}\cdot\boldsymbol{u}$ and $\boldsymbol{u}$ is the Eulerian current velocity. It is approximated by

$$\mathcal{K}_a \approx \frac{1}{4}\frac{\sigma A_f^2}{k_p\sinh^2 k_p\,D}\int_{-h}^{\eta+\hat{\eta}} \frac{\partial^2 \mathcal{V}}{\partial z^2}\sinh[2k_p(z'-z)]dz, \tag{40}$$

with $\boldsymbol{k}_p = k_p(\cos\overline{\theta}, \sin\overline{\theta})$. Following UMS10, the leading order quasi-static pressure is given by

$$\mathcal{P} = \frac{gA^2}{2\sigma}\left\{\frac{\tanh[\mathcal{H}]}{\sinh[2\,\mathcal{H}]}\left(-\frac{\partial\mathcal{V}}{\partial z}\Big|_{\eta+\hat{\eta}} + \cosh[2\,\mathcal{H}]\frac{\partial\mathcal{V}}{\partial z}\Big|_{-h} + \int_{-h}^{\eta+\hat{\eta}}\frac{\partial^2\mathcal{V}}{\partial z^2}\cosh[2\,k\,z]dz\right) - 2k\tanh[\mathcal{H}]\mathcal{V}|_{\eta+\hat{\eta}}\right\}, \tag{41}$$

where $\mathcal{H} = k\,D$. The first and third pressure terms can only be finite in intermediate and shallow water because of the $\tanh[2\,\mathcal{H}]/\sinh[2\,\mathcal{H}]$ factor and therefore are approximated with the filtered long-wave information (A_f and k_p). The second term is approximated with k_p but with the total wave amplitude A_w. And the fourth pressure term is approximated with the surface Stokes drift and the two-scales, k_e and k_p. The complete pressure approximation for the four terms is given by

$$\begin{aligned}\mathcal{P}_a \approx & \underbrace{-G(\mathcal{H}_p,\sigma)A_f^2\frac{\partial \mathcal{V}}{\partial z}\Big|_{\eta}}_{\mathcal{P}_1} + \underbrace{G(\mathcal{H}_p,\sigma)A_w^2\cosh[2\,\mathcal{H}_p]\frac{\partial \mathcal{V}}{\partial z}\Big|_{-h}}_{\mathcal{P}_2} \\ & \underbrace{+G(\mathcal{H}_p,\sigma)A_f^2\int_{-h}^{\eta+\hat{\eta}}\frac{\partial^2 \mathcal{V}}{\partial z^2}\cosh[2\,k_p\,z]dz}_{\mathcal{P}_3} \underbrace{-2\,M(k_p,k_e)\boldsymbol{u}_s\cdot\boldsymbol{u}\Big|_{\eta+\hat{\eta}}}_{\mathcal{P}_4},\end{aligned} \tag{42}$$

where $G(\mathcal{H}_p,\sigma) = \frac{g}{2\sigma}\frac{\tanh[\mathcal{H}_p]}{\sinh[2\,\mathcal{H}_p]}$, $\mathcal{H}_p = k_p\,D$, and $M(k_p,k_e)$ is a non-dimensional function that smoothly connects the deep-water and shallow-water regimes according to

$$M(k_p,k_e) = \frac{\sinh^2[k_eD]}{\cosh[2k_eh]}\tanh[k_ph] + \frac{\sinh^2[k_pD]}{\cosh[2k_ph]}(1-\tanh[k_ph]). \tag{43}$$

In deep-water ($k_pD > 2\pi$), the last term in (42) becomes $-\boldsymbol{u}_s\cdot\boldsymbol{u}\big|_{\eta}$, whereas in shallow-water ($k_pD < \pi/10$) it matches the monochromatic approximation ((41), fourth term) in terms of A_w and k_p.

For the sake of comparison, we also consider the spectral reconstruction approach proposed by Kumar et al. (2017) to compute the WEC forcing. The wave spectral reconstruction is based on the premise that given a few parameters (energy, mean period and direction, and possibly other spectral moments) directional wave spectra can be reconstructed based on empirical models. The reconstruction can include a combination of different wave systems, for example mixed wind-sea and swell. Kumar et al. (2017) proposed the use of the JONSWAP spectrum and the spectral partition information from WW3 to reconstruct the directional spectrum from which WEC forcing can be computed by ocean circulation models. The spectral reconstruction is computationally expensive and not necessarily more accurate as demonstrated here.

2.3. Non-conservative WEC effects

Here we consider the energy and momentum flux due to surface wave breaking. The flux of energy due to wave breaking enhances the vertical mixing near the surface, which is commonly modeled with various turbulence closure schemes (Craig and Banner, 1994; Terray et al., 1999; Burchard, 2001; Umlauf and Burchard, 2003). We model the vertical mixing due to wave breaking K_{br} directly as a near-surface enhancement of the K-Profile Parameterization (KPP, Large et al., 1994) by generalizing the framework introduced by UMS10 for both white-capping and depth-limited breaking. UMS10 prescribed several profiles for $K_{br}(z)$ in shallow water that were constrained by a depth-average diffusivity $\overline{K}_{br} = c_b\frac{H_s}{\sqrt{2}}(\frac{E_{ds}}{\rho_w})^{1/3}$, where c_b is a dimensionless factor O(0.1), E_{ds} is the flux of energy due to wave breaking, and ρ_w is the water density. The vertical profiles were designed for shallow water and therefore are not immediately applicable for deep-water wave breaking. We follow a different approach.

Our starting point is the empirical scaling of the turbulent kinetic energy (TKE) dissipation profile $\epsilon(z)$ by Sutherland and Melville (2015), hereafter referred to as SM15, based on H_s and the energy flux due to wave breaking E_{ds} according to

$$\epsilon\frac{H_s\rho_w}{E_{ds}} \equiv \epsilon_n = f(z'), \tag{44}$$

where ϵ_n is the non-dimensional dissipation rate, ρ_w is the water density and $z' = Z/H_s$ is the non-dimensional depth, with $Z = (z-\eta-\hat{\eta})$ being the depth from the surface. SM15 reported two power-law regimes, $\epsilon_n \sim z'^{-2}$ for $z' < 1$ and $\epsilon_n \sim z'^{-1}$ closer to the surface. Eq. (44) differs from the scaling by Terray et al. (1996), which is in terms of the wind input as opposed to the dissipation due to breaking. The input of TKE due to breaking E_{ds}/ρ_w is often parameterized as $m\,u_{w*}^3$, with u_{w*} corresponding to the water-side friction velocity and $m = 100$ (Craig and Banner, 1994). More recently, Esters et al. (2018) reported TKE dissipation rate measurements collected with a vertical profiles over a wide range of conditions. Their measurements did not capture the enhancement of ϵ near the surface, which could be in part because their data did resolve the dissipation profile very near-surface (i.e., $z/H_s > 1$). They reported a single power-law dependence of $\epsilon \sim z^{-3/2}$.

We model the nondimensional TKE dissipation profile according to

$$f(z') = \frac{0.9508}{(A_f - B_f\,z' + C_f\,z'^2)}, \tag{45}$$

with $A_f = 4/30$, $B_f = 8/3$, and $C_f = 10/3$ such that $\int_{-3}^{0} f(z')dz' = 1$, approximately matching SM15. Eq. (45) can be used to model the dissipation profile $\epsilon(z)$ provided E_{ds} and H_s are known. For a given turbulent length scale ℓ and TKE dissipation ϵ, the eddy viscosity K is often parameterized as

$$K \equiv (\epsilon\ell)^{1/3}\ell. \tag{46}$$

Following Terray et al. (1999), we prescribe the turbulent length scale with a linear profile according to

$$\ell(z) = \begin{cases} \kappa z_o, & |z| \le z_o \\ \kappa|z|, & |z| > z_o \end{cases} \tag{47}$$

where κ is the von Kármán constant, z_o is the roughness length. The surface roughness length z_o is commonly parameterized as $z_o = A\,H_s$, with A being a constant between 0.2 and 1 (Terray et al., 1999; Burchard, 2001). We use $A = 0.6$, which is consistent with Moghimi et al. (2016).

Finally, we parameterize the vertical mixing due to wave breaking K_{br} with Eqs. (45)–(47), including a tapering function $\mathcal{T}(z') = 1 - \tanh^4(z')$ approaching zero for $z' > 3$. The complete parameterization of K_{br} becomes

$$K_{br}(z) = \mathcal{T}(z)\,\epsilon(z)^{1/3}\ell^{4/3}, \tag{48}$$

which is added to KPP for both the momentum and scalar diffusivities. We do not distinguish between mixing due to white-capping in deep water and depth-induced breaking. Our approach is suitable for both deep and shallow wave breaking, giving depth-averaged diffusivities

$$\overline{K}_{br} = \int K_{br}(z-\eta)dz \Big/ \int dz \tag{49}$$

$$\approx 0.1\left(\frac{E_{ds}}{\rho_w}\right)^{1/3} H_s, \tag{50}$$

for $z - \eta > \max(-h, -2H_s)$, which is larger than that of USM10 by a factor of $\sqrt{2}$. The breaking diffusivity model of USM10 consists $K_{br}(z) = c_{br}\left(\frac{E_{ds}}{\rho_w}\right)^{1/3} H_{rms}\,F^{br}$, where $H_{rms} = H_s/\sqrt{2}$ is the root-mean-square wave height, F^{br} is a prescribed vertical structure normalized such that $\int_{-h}^{\eta+\hat{\eta}} F_{br}(z')dz' = 1$, and c_{br} is a non-dimensional scaling factor O(0.1). USM10 considered three arbitrary types of vertical structures $F_{br}(z')$ with different decay rates. In shallow water, our approach differs from USM10 in terms of the vertical structure and in magnitude by a factor of $\sqrt{2}$, which is consistent with the different wave breaking height scaling parameters (H_s vs. H_{rms}).

Based on the conservation of momentum, the momentum flux vector at the ocean surface is given by

$$\boldsymbol{\tau}_{oc} = \boldsymbol{\tau}_{ds} + \boldsymbol{\tau}_u, \tag{51}$$

where $\boldsymbol{\tau}_{ds} = -\rho\,g\iint S_{ds}(f,\theta)\boldsymbol{k}\,\sigma^{-1}df\,d\theta$ is the resolved momentum flux due to breaking in deep water, $S_{ds}(f,\theta)$ is the spectral energy dissipation due to breaking, and $\boldsymbol{\tau}_u$ is the momentum flux supported by tangential stress and the unresolved part of the wave spectrum. The

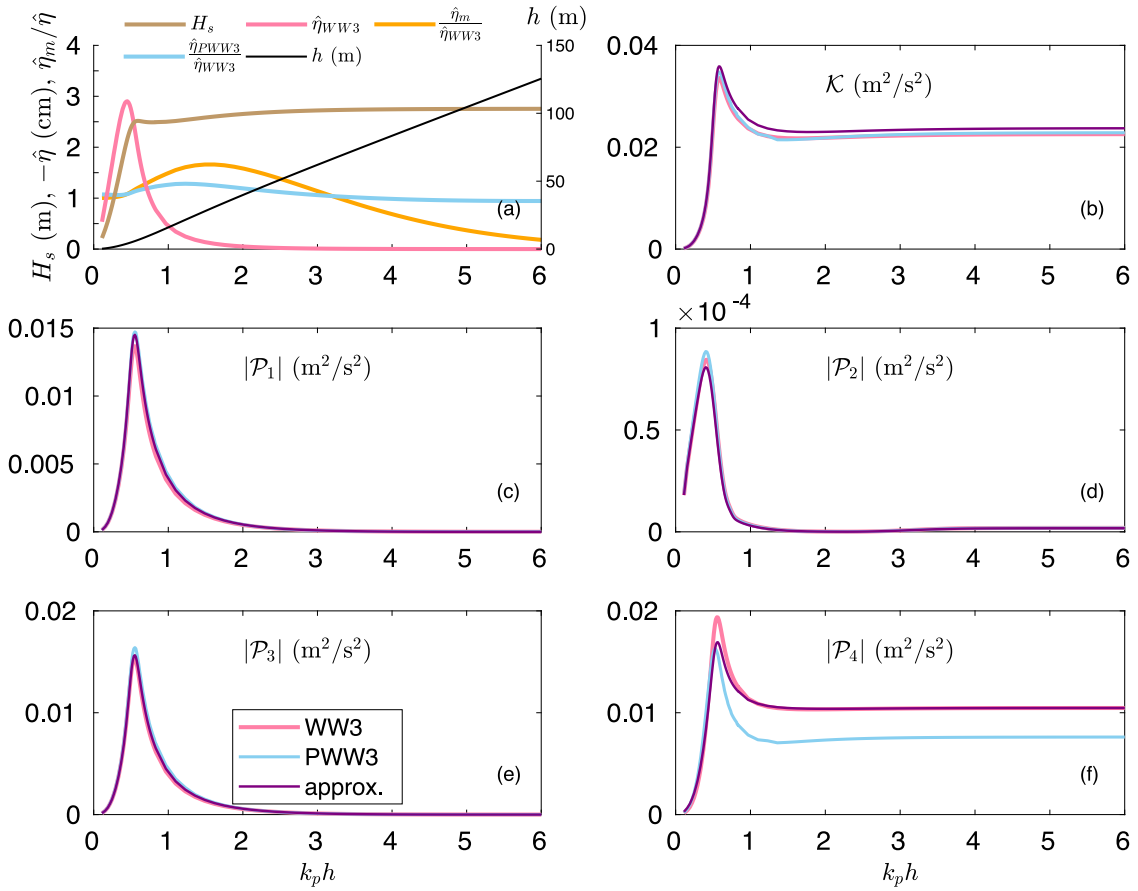

Fig. 1. Results for the idealized shoaling wave spectrum plotted as function $h\,k_p$ with the shore on the left. (a) Significant wave height, set-down $-\eta$, the ratio $\hat{\eta}_m/\hat{\eta}$, and water depth h, (b) Bernoulli head $\mathcal{K}$ and (c–f) pressure $\mathcal{P}$ terms (42). The pink, blue, and purple lines are the estimates using the directional wave spectra (WW3), the spectral reconstruction (PWW3), and approximations, respectively.

latter can be obtained from the momentum conservation equation on the air-side $\boldsymbol{\tau}_a = \boldsymbol{\tau}_w + \boldsymbol{\tau}_u$, with $\boldsymbol{\tau}_a$ corresponding to the total wind stress, and $\boldsymbol{\tau}_w = \rho\, g \iint S_{in}(f,\theta)\mathbf{k}\,\sigma^{-1} df d\theta$ is wave-induced stress. Therefore, the ocean-side stress can be written as

$$\boldsymbol{\tau}_{oc} = \boldsymbol{\tau}_a - (\boldsymbol{\tau}_w - \boldsymbol{\tau}_{ds}), \tag{52}$$

which is consistent with Breivik et al. (2015) and Wu et al. (2019). For winds and waves in equilibrium $\boldsymbol{\tau}_w \approx \boldsymbol{\tau}_{ds}$, thus $\boldsymbol{\tau}_{oc} \approx \boldsymbol{\tau}_a$, which corresponds to the common assumption used for ocean models. The ocean-side stress becomes smaller than the wind stress for developing waves, and can exceed τ_a for decaying winds. Similarly, $\boldsymbol{\tau}_{oc}$ can deviate in direction from $\boldsymbol{\tau}_a$ for conditions of misaligned winds and waves. In this study as discussed in Section 2.5.2, $\boldsymbol{\tau}_{oc}$ is approximated as $\boldsymbol{\tau}_a$ since their magnitude difference is generally small but is introduced here for completeness. We note that Staneva et al. (2017) reported significant differences on storm surge levels produced in the North Sea by $\boldsymbol{\tau}_{oc}$ compared to $\boldsymbol{\tau}_a$.

2.4. Idealized shoaling waves

The wave approximations were tested with an idealized wave shoaling experiment using WW3. The shoaling wave test case of WW3 (tp1.8) consisting of a linear 1 km long beach profile out to 12 m water depth was extended 5 km further offshore with a quadratic shelf profile out to a water depth of 400 m. The offshore boundary conditions were specified with a directional wave spectrum from an idealized wind-forced solution close to wind-wave equilibrium with 10 m/s winds (Romero, 2019) and $H_s = 2.6$ m. The wave spectrum was allowed to propagate toward the beach without wind forcing. Bottom friction (Ardhuin et al., 2003) and depth-induced breaking (Battjes and Janssen, 1978) were activated with no other source terms. Directional spectra were saved at selected locations and used to test the WEC forcing approximations offline. Wave solutions did not include current effects on waves. The purpose of this experiment was to demonstrate the various approximations for an idealized shoaling broadband wave spectrum starting from deep water. The current profiles used for the computations of the pressure and the Bernoulli head are $u(z) = -u_s(z)$, for convenience because $u_s(z)$ has non-zero second derivatives needed for some of the terms.

The significant wave height H_s, set-down $\hat{\eta}$, and $\hat{\eta}_m/\hat{\eta}$ are plotted as a function of the water depth scaled by k_p in Fig. 1a. The wave height decreases sharply in shallow-water due to depth-induced breaking and bottom friction. The monochromatic set-down $\hat{\eta}_m$ is larger than the broadband value for $1 < k_p h < 2$, where $\hat{\eta}$ is small but finite. The set-down calculated from the spectral reconstruction (PWW3) is in good agreement with direct computations with a small positive bias ($\sim$ 20%). The Bernoulli head (39) and pressure (41) generalized for a wave spectrum given by

$$\mathcal{K} = \frac{1}{2} \iint \frac{\sigma \Psi(f,\theta)}{k \sinh^2 k\, D} \int_{-h}^{z} \frac{\partial^2 \mathcal{V}}{\partial z'^2} \sinh[2k(z-z')] dz' df d\theta \tag{53}$$

and

$$\mathcal{P} = g \iint \frac{\Psi(f,\theta)}{\sigma} \left\{ \frac{\tanh[\mathcal{H}]}{\sinh[2\,\mathcal{H}]} \left(-\frac{\partial \mathcal{V}}{\partial z}\Big|_{\eta+\hat{\eta}} + \cosh[2\,\mathcal{H}] \frac{\partial \mathcal{V}}{\partial z}\Big|_{-h} + \int_{-h}^{\eta+\hat{\eta}} \frac{\partial^2 \mathcal{V}}{\partial z'^2} \cosh[2\,k\,z] dz \right) - 2k \tanh[\mathcal{H}] \mathcal{V}|_{\eta+\hat{\eta}} \right\} df d\theta. \tag{54}$$

computed from the resolved spectrum and spectral reconstruction are plotted against $k_p\,h$ in Fig. 1b–f. The pressure terms magnitudes (1–4)

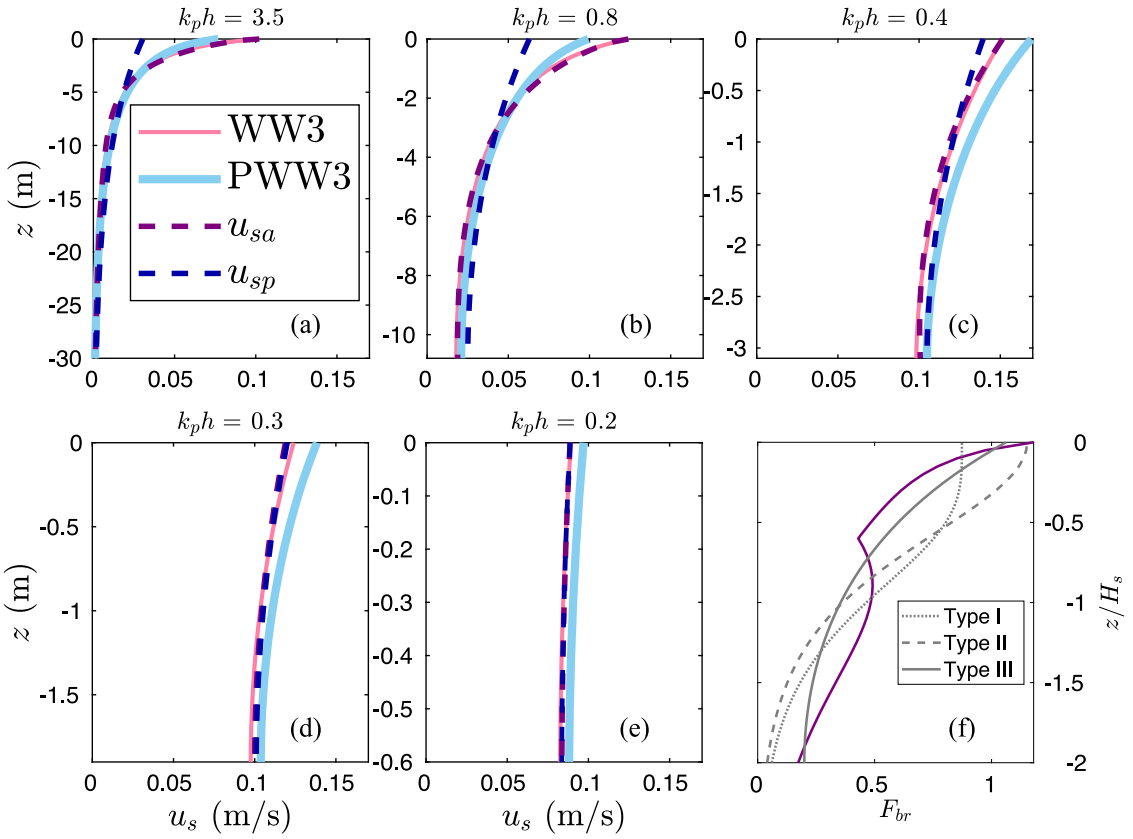

Fig. 2. Stokes drift profiles for the idealized wave shoaling solution from deep to shallow water with k_ph varying between 3.5 and 0.2 (a–e) comparing direct broadband computations (WW3) against the approximation u_{sa}, the spectral reconstruction (PWW3), and the monochromatic approximation u_{sp}. (f) Nondimensional breaking diffusivity profile $F^{br}(z) = K_{br}(z)/\overline{K}_{br}$ calculated from K_{br} in equation ((48) - solid purple line) compared to the three types considered by UMS10.

are plotted separately in panels (c–f). The corresponding approximations (40) and (42) shown in purple and estimates from the spectral reconstruction (PWW3) shown in blue, are in good agreement with the direct computations, with relatively small differences. The spectral reconstruction gives the largest difference for $\mathcal{P}_4$ with a negative bias of 30% in intermediate and deep-water. All pressure terms and Bernoulli head have maxima in shallow water, with $\mathcal{K}$ and $\mathcal{P}_4$ being dominant in deep-water. The corresponding Stokes drift profiles computed from the resolved directional spectra and spectral reconstruction are compared to the approximation in Fig. 2 for water depths varying from deep ($k_ph > \pi$) to shallow ($k_ph < \pi/10$) in panels (a–e). The Stokes drift approximation accurately reproduces the broadband computations with small deviations near the surface at $k_p h = 0.3$ (e). The spectral reconstruction gives errors up 20% in magnitude, with larger errors near the surface. The monochromatic approximation misses the shear intensification near the surface for $k_p h > 0.3$.

The shoaling waves analysis is complemented by the analyzing structure of the vertical diffusivity due to wave breaking in shallow water. We compare the different vertical structures of $F_{br}(z) = D^{-1}\int K_{br}(z')dz'$ computed from Eq. (48) against the three types of vertical structures considered by USM10 in Fig. 2f. The vertical structure of (48) is most similar to the structure Type III of UMS10 with relatively strong decay near the surface. In contrast, structures Type I and II show more gradual decay near the surface. Although the different structures differ in shape, all four show qualitatively similar trends over the depth range of twice H_s.

2.5. Regional model configuration

The coupling framework is evaluated with WW3 and implemented in ROMS building on the work by UMS10. We used an existing nested configuration in Southern California with a horizontal resolution of 270 m (see Figure 1 in Romero et al., 2020).

2.5.1. Wave model

The WW3 solutions from Romero et al. (2020), hereafter referred to as RHM20, were used to evaluate the coupling framework offline. The solutions cover two one-month-long periods in the Winter 2006 and Spring 2007. The winter period included periods of strong winds and relatively large waves, with surface winds reaching 18 m/s and H_s up to 8.5 m in the open ocean. The model configuration includes realistic bathymetry and wind forcing from the Weather Research and Forecasting (WRF) model (Renault et al., 2016). The wave model was constrained with buoy observations through boundary conditions and validated against independent buoys within the domain as described in RHM20. The wave model was forced with the wind input by Ardhuin et al. (2010), the discrete interaction approximation of the nonlinear energy fluxes (Hasselmann and Hasselmann, 1985), the saturation-based wave breaking dissipation by Romero (2019), and bottom dissipation of Ardhuin et al. (2003). Available wave directional spectra at seven different buoy locations (Diablo Canyon, Harvest, Goleta, Rincon, Anacapa, Santa Monica and San Pedro — see Fig. 1 in RHM20) in water depths between 550 and 20 m for the two periods were used to evaluate the wave approximations. We used the corresponding ROMS current profiles from RHM20 at the buoy locations for the offline computation and validation of the pressure and Bernoulli head.

2.5.2. Ocean model

The wave approximations and parameterization of the vertical mixing due to breaking waves described in Sections 2.2 and 2.3 were implemented and tested in ROMS with the 270 m resolution configuration in Southern California (Renault et al., 2016; Dauhajre et al., 2019; Romero et al., 2020), which includes realistic bathymetry, tides, and forcing from WRF. The vertical grid has 50 levels in terrain-following

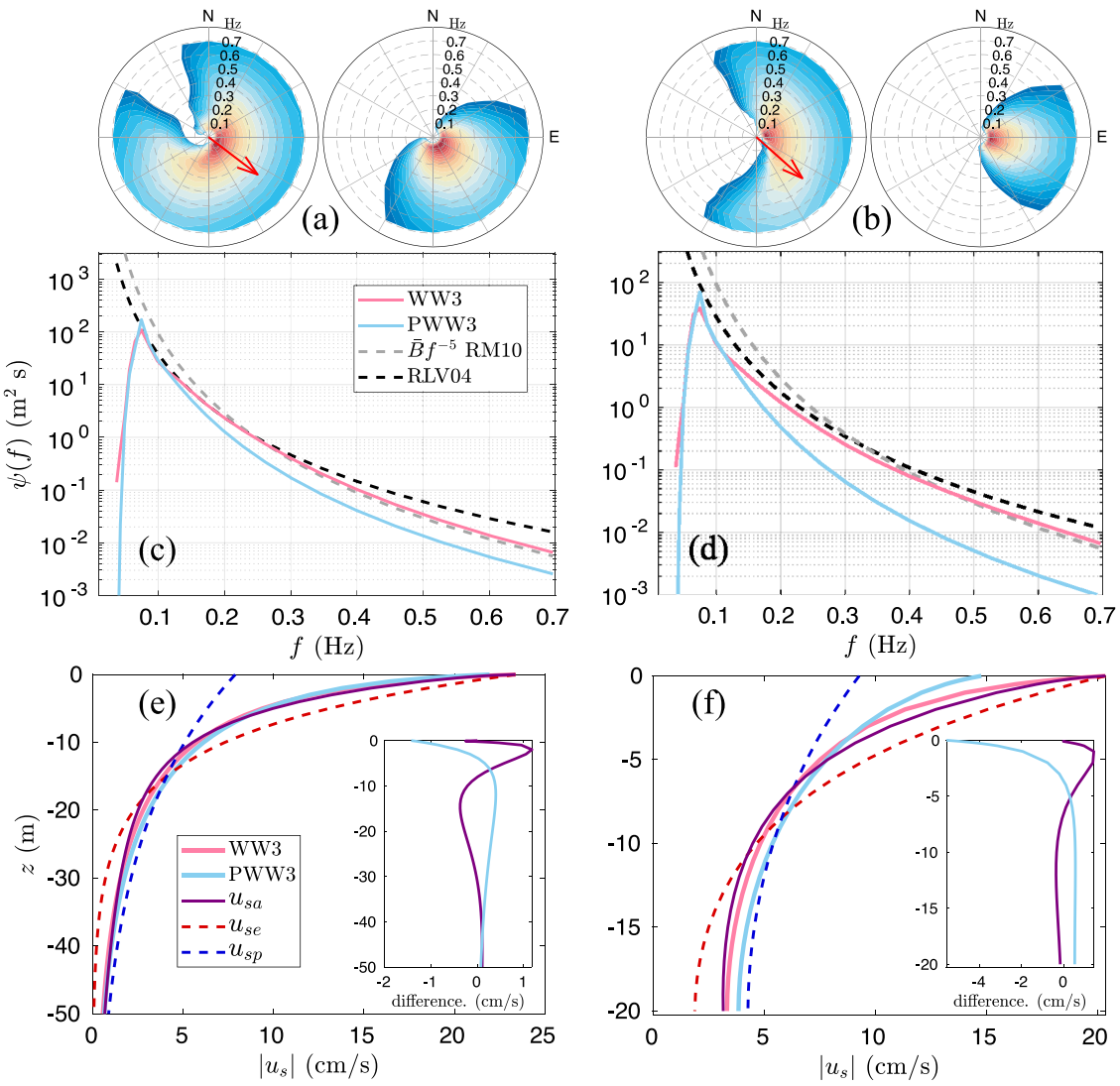

Fig. 3. Examples of two cases during a large wave event with wave spectra with a single peak at Harvest (left panels, $h = 550$ m) and Diablo Canyon (right panels, $h = 20$ m) on December 28, 2006, at 00:00 h (UTC) during a storm. The significant wave height is 8 and 5 m and the wind speed 19 and 15 m/s, respectively. (a, b) Directional spectra from WW3 solutions (left sub-panels) and spectral reconstruction PWW3 (right sub-panels). The red arrows shows the wind direction. Spectra are plotted with the oceanographic convention (energy going toward). (c, d) Azimuth integrated spectra (pink) from WW3 and the reconstruction (PWW3 — blue). The saturation level from Romero and Melville (2010) and the equilibrium range level by Resio et al. (2004) are shown with dashed lines in gray and black, respectively. (e, f) Stokes drift profiles computed from the broadband WW3 spectra (pink) and the spectral reconstruction (light blue) compared to the approximation (u_{sa}, purple) and its constituents (u_{se} and u_{sp} in dashed red and dark blue, respectively). Notice that in panel (e) the pink line is not visible as it lies below the purple line. The insets in (e) and (f) show the differences relative to WW3.

or sigma coordinates with vertical grid cell refinement near the surface and the bottom. The wave forcing was generated offline from a WW3 solution identical to that described in Romero et al. 2020 except for the addition of tidal forcing from non-WEC ROMS output through changes in water elevation.

To avoid unphysically large waves at the coast for our relatively coarse ROMS model, particularly around islands with abrupt changes in water depth, WW3 included depth-induced breaking dissipation (Battjes and Janssen, 1978). This was further supplemented offline with a depth-dependent wave height limiter according to

$$H_s = \min[\gamma\, D, H_s] \tag{55}$$

with $\gamma = 0.78$ (WW3DG). Similarly, the online computed Stokes drift transport, surface Stokes drift and wave set-down were also scaled offline by a limiting factor F^2, with $F = \min(1, \gamma D/H_s)$ calculated prior to applying the limiter (55). The power of two for the factor F^2 is dimensionally consistent with the dependence of the Stokes drift and set-down on the wave amplitude squared. The γ factor helped maintain numerical stability at the coastline but not everywhere. Enabling the depth-limited breaking diffusivity, even for this relatively coarse model grid, is by far the most effective way to maintain numerical stability and reasonable integration times steps without violating the CFL condition in ROMS. All WEC runs include both the limiter and the depth-limited wave breaking diffusivity. Note that the waves do not vanish at the boundary, which has to be accounted for in the boundary conditions of ROMS at the land interface by imposing zero normal Lagrangian flow.

The ROMS boundary conditions at the shore are free slip and zero normal flux for non-WEC and zero normal Lagrangian flux for WEC with $u(z) = -u_s(z)$. Open boundaries of the outgoing barotropic flow and surface elevation use shallow gravity wave radiation conditions (Flather, 1976; Chapman, 1985), and the tangential barotropic velocities use an Orlanski radiation condition (Orlanski, 1976). Orlanski-type radiation boundary conditions are also used for the baroclinic fields, including tracers, but with additional nudging toward the parent solution (Marchesiello et al., 2001; Mason et al., 2010). We subtracted the normal Stokes drift at the boundary from the inflow of the non-WEC parent used for the nudging of the WEC run. Following Kumar et al. (2015), the outgoing baroclinic flow and tracers

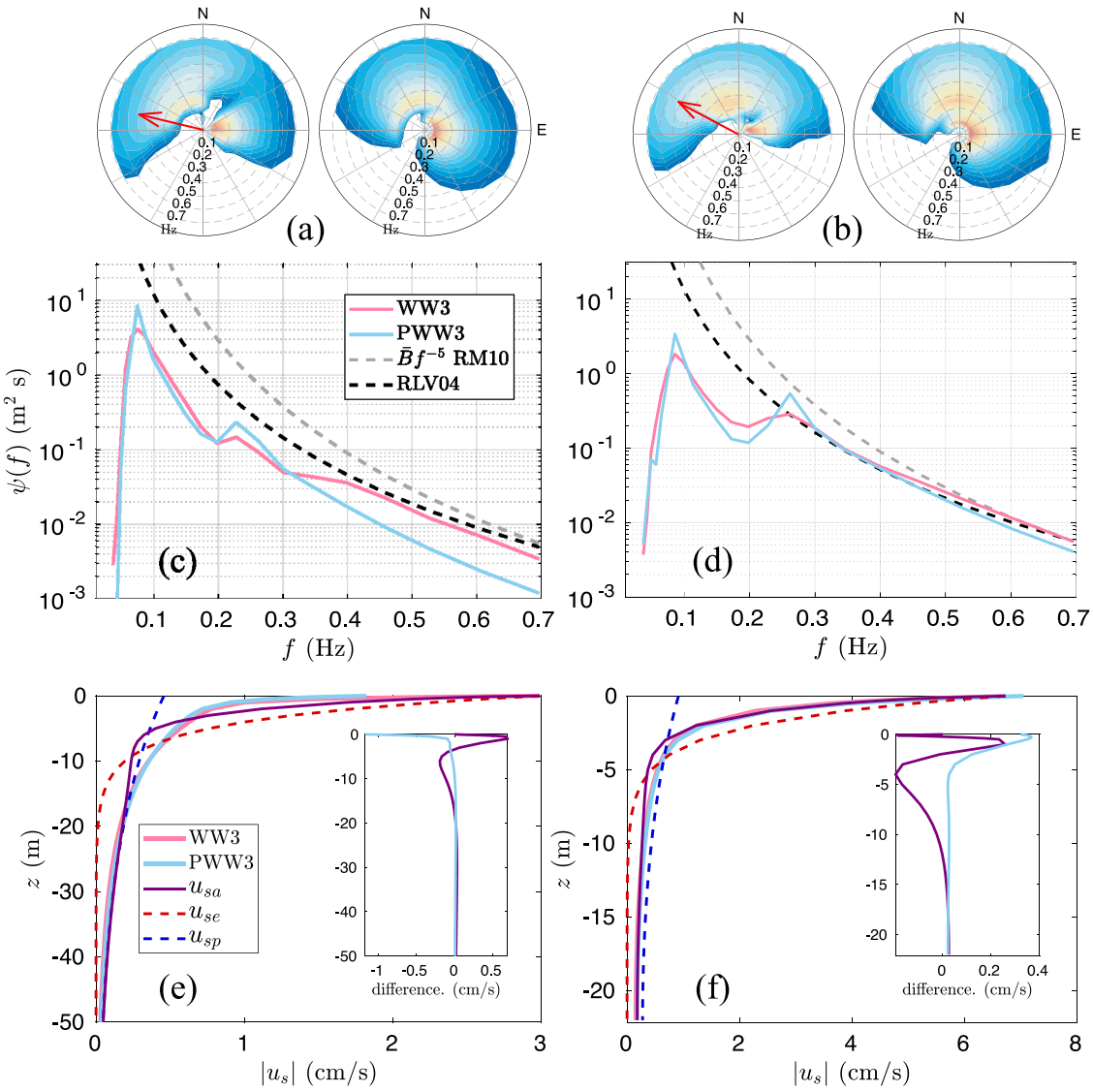

Fig. 4. (a, d) Examples of mixed wave spectra at San Pedro ($h = 472$ m, left) and Rincon ($h = 22$ m, right) on December 10, 2006, at 03:00 h (UTC). The significant wave height is 1.9 and 1.4 m and the wind speed 6.0 and 7.5 m/s, respectively. (a, b) Directional spectra from WW3 solutions (left sub-panels) and spectral reconstruction PWW3 (right sub-panels). The red arrows shows the wind direction. (c, d) Corresponding azimuth integrated spectrum (pink) compared to the reconstruction PWW3 (blue). The saturation level from Romero and Melville (2010) and the equilibrium range level by Resio et al. (2004) are shown with dashed lines in gray and black, respectively. (e, f) Stokes drift vertical profiles from the broadband spectrum (pink) and the spectral reconstruction (light blue) compared to the approximation (u_{sa}, purple). The insets in (e) and (f) show the differences relative to WW3.

were weakly nudged with a time scale of 360 days, while the incoming normal flow and tracers are strongly nudged with a time scale of 30 min. We carried out several tests with longer nudging time scales for the incoming flow and tracers which resulted in spurious and apparent artifacts at the boundaries of the WEC solutions. For comparison, the control (non-WEC) run was also tightly nudged despite the fact that weakly nudged non-WEC solutions behave reasonably near the boundaries. Sponge layers of 40 grid cells with a horizontal diffusivity linearly decreasing from 5 m^2/s at the boundary to zero in the interior were used for both WEC and non-WEC runs.

ROMS vertical mixing is parameterized with the K-Profile Parameterization (KPP, Large et al., 1994; Durski and Haidvogel, 2004). The non-breaking wave-induced mixing from the time derivative of mean particle displacement variance k_{vw}, Eq. (26), was included as an additional source of mixing although it is several orders of magnitude smaller than KPP, except at the surface where KPP is zero. As mentioned before, all WEC runs included vertical mixing due to depth-limited breaking to help maintain numerical stability at the coastline, particularly for the vertical CFL condition. Deep-water breaking diffusivity was not included, except in one of the runs. Additional sources of WEC mixing due to bottom-drag are not considered in this study. Comparisons between $\boldsymbol{\tau}_{oc}$ and $\boldsymbol{\tau}_a$ based on offline computations from WW3 solutions at the buoy locations indicated that in general $\boldsymbol{\tau}_{oc} \approx \boldsymbol{\tau}_a$ is a good approximation with a few percent in magnitude except in certain areas close to the shore reaching differences of up to 10% in magnitude due spatial inhomogeneities of the winds. For the surface momentum flux in ROMS we assume wind-wave equilibrium (i.e., $\boldsymbol{\tau}_{oc} = \boldsymbol{\tau}_a$) and $\boldsymbol{\tau}_a$ is computed with the bulk formulation described in Large and Yeager (2004) and Large (2006). Eq. (52) is introduced in Section 2.3 for completeness. For general applications $\boldsymbol{\tau}_a$ should be computed from the wave model accounting for sea state or wave age dependence and S_{in} should account for atmospheric stability effects including humidity (ECMWF, 2013). Table 1 summarizes the different model solutions based on the forcing, which are (1) a control (CTL) without WEC, (2) spectral peak monochromatic WEC (WECM)

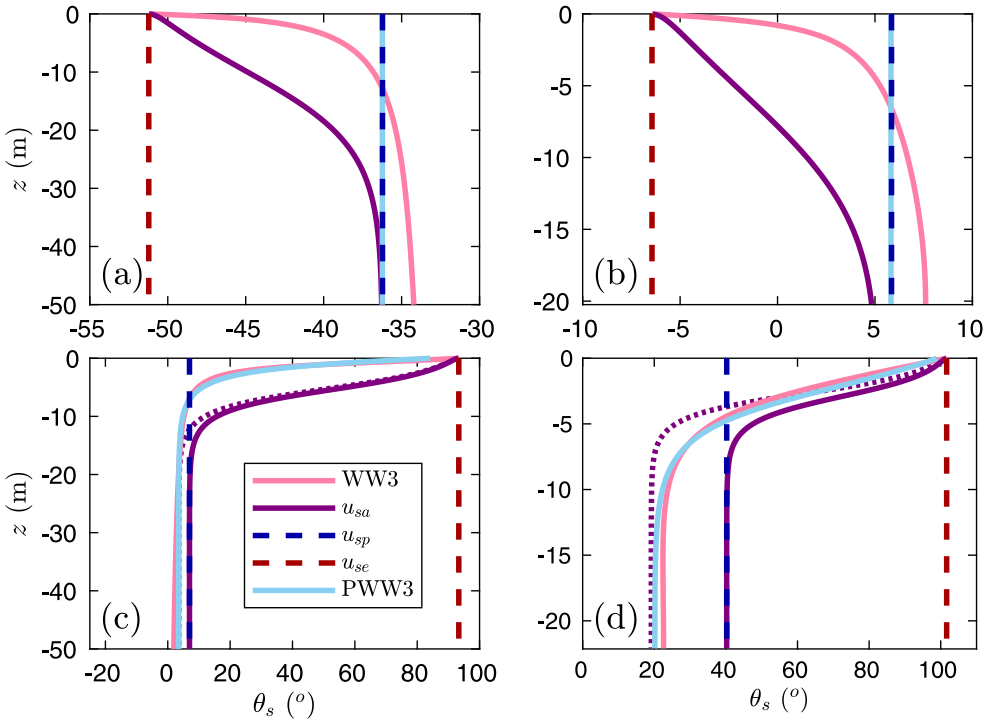

Fig. 5. Vertical profile of the Stokes drift direction $\theta_s(z)$ for the cases shown in Figs. 3 and 4, corresponding to panels (a, b) and (c, d), respectively. The pink, purple, and blue solid lines correspond to the spectral estimate (WW3), the approximation, and that from the spectral reconstruction (PWW3). The constituents of the approximation u_{se} and u_{sp} are shown in dashed red and dark blue, respectively. The purple dotted line is the approximation using the mean swell direction from the spectral reconstruction for the long wave information instead of $\bar{\theta}$, significantly improving the approximation direction at depth.

Table 1
Summary of the solutions labeled according the forcing, including the control without WEC and the three separate WEC runs considered.

Run	WEC	Monochromatic	Broadband	Deep-Water K_b
CTL				
WECM	✓	✓		
WECB	✓		✓	
WECBK$_b$	✓		✓	✓

corresponding to UMS10, (3) broadband WEC forcing within the framework here described (WECB), and (4) WECB with near-surface vertical mixing due to breaking enabled (WCBK).

3. Results

The results are divided into two subsections: (1) analysis of the wave approximations and parameterization of the vertical mixing due to wave breaking, and (2) analysis of ROMS WEC solutions compared to a control without wave forcing.

3.1. Stokes drift

We begin this subsection by comparing the Stokes drift approximation against broadband computations using the resolved directional spectrum from the WW3 regional configuration in California. For the sake of comparison, we also analyze the Stokes drift obtained with the spectral reconstruction approach proposed by Kumar et al. (2017). Examples during a strong wind/wave event in deep (550 m) and shallower water depth (20 m) are shown in Fig. 3, left and right panels, respectively. The resolved directional spectra (left sub-panels) are compared against the spectral reconstruction according to Kumar et al. (2017) (right sub-panels), referred to as PWW3 following their labeling. The directional spectrum reconstruction (PWW3), is narrower than the resolved spectrum. The corresponding azimuth integrated spectra $\psi(f) = \int \psi(f,\theta)\, d\theta$ are shown in Figs. 3c, d. The resolved 1d spectrum in pink shows a tail of approximately f^{-5} within the level observed by Romero and Melville (2010) and Lenain and Melville (2017). In contrast, the reconstructed spectrum (PWW3) decays much faster with increasing frequency, particularly for the shallower case.

The resulting vertical Stokes drift profiles in 3e, f show the spectral reconstruction is missing a significant fraction of the Stokes drift near the surface for the shallower water case (panel f) because of the lower energy levels of the spectrum at higher frequencies. The Stokes drift approximation from this study u_{sa} is shown in purple, accurately matching the broadband computations in deep water (e), with small but noticeable errors for the shallower water case (f). As described in Section 2.1, the approximation u_{sa} is composed of two parts: (1) u_{se} which is based on a vertical scale constrained by the known surface Stokes drift and Stokes transport, and (2) u_{sp} calculated using the peak wavenumber, significant wave height and mean wave direction. The two components u_{se} and u_{sp} are smoothly combined with a ramp function yielding u_{sa}. Both u_{se} and u_{sp} are shown in Fig. 3e, f with dashed red and blue lines, respectively. The component u_{se} matches the pink curve at the surface by design but decays much faster with depth for $z < -10$ m. In contrast, the monochromatic approximation u_{sp} based on the spectral peak information better matches the pink line at depth, strongly underestimating the Stokes drift near the surface. The resulting blended approximation u_{sa} giving more weight to u_{se} near the surface and u_{sp} at depth does a good job matching the profiles computed from directional wave spectra (WW3).

Examples of complex spectra during mixed wind-sea and swell with strong misalignment are shown in Fig. 4 in deep (472 m, left panels) and shallower water depth (22 m, right panels). The two spectral peaks can be clearly seen in the directional spectra (a, b) from both WW3 and the spectral reconstruction (PWW3) with an angle separation of 90 degrees or more. The directional spreading of the swell band is larger in reconstruction compared to that of the resolved spectra. The corresponding 1D spectra clearly show the two peaks of the wind-sea and the swell, with the latter containing most of the energy. For this case

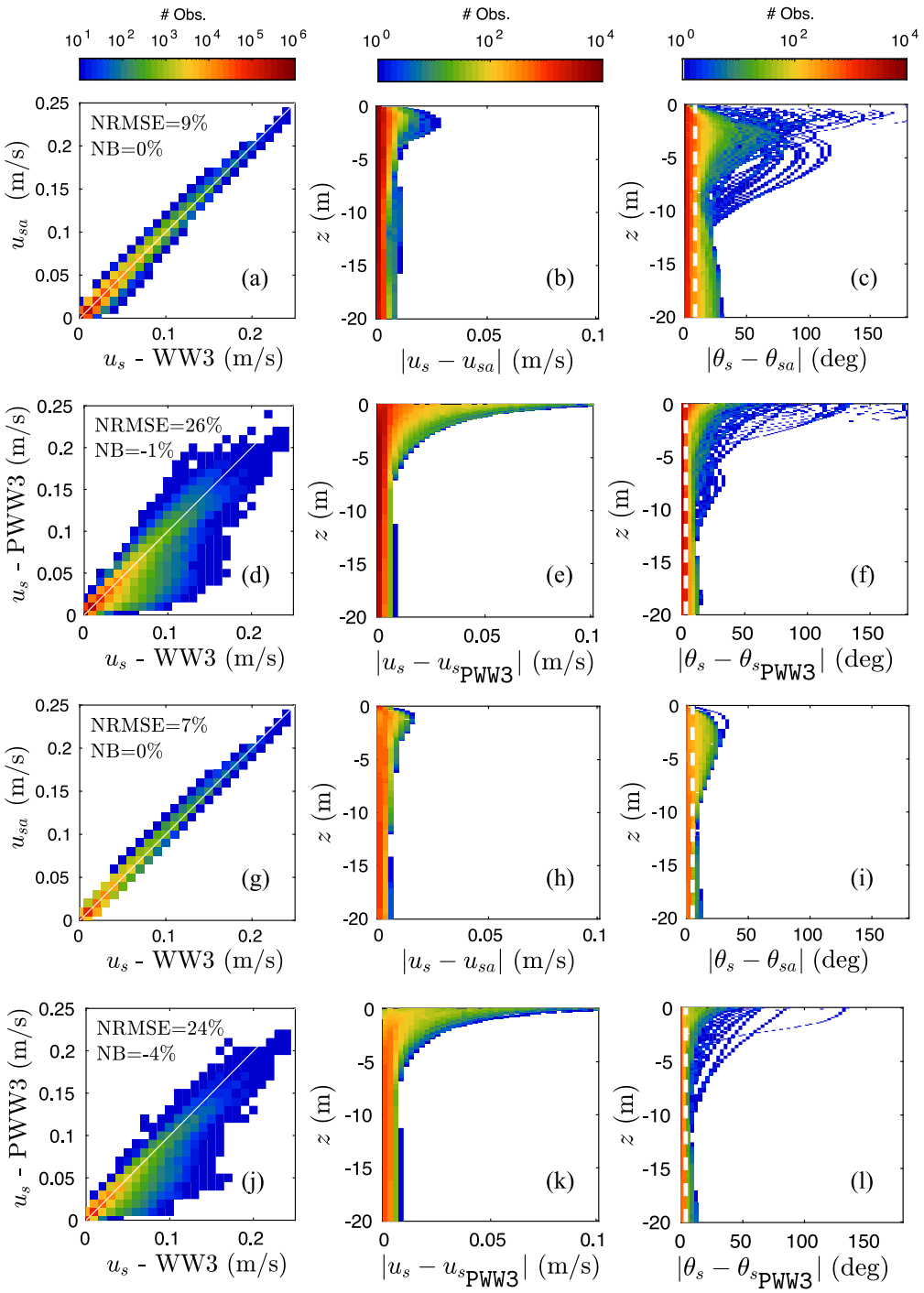

Fig. 6. Scatter plots of the Stokes drift amplitude comparing the approximation (a) and the spectral reconstruction (PWW3 — d) against the broadband computations (WW3) during two one-month-long periods the Winter 2006 and Spring 2007. The corresponding absolute deviations for Stokes drift amplitude and angle are plotted vs. depth in (b, e) and (c, f), respectively. The same set of plots for cases without swell (wind-sea only) are shown in (g–l).

of weak wind forcing, the WW3 spectra (pink) show a tail consistent with the equilibrium spectrum of $\propto f^{-4}$ by Resio et al. (2004). Under weak wind forcing the spectrum would be expected to transition to a saturation regime of f^{-5} at higher frequencies not resolved by the model (Romero and Melville, 2010; Lenain and Melville, 2017; Romero, 2019). The reconstructed spectrum (blue) decays much faster with increasing frequency in panel (c) underestimating the Stokes drift near the surface (e). In contrast, PWW3 overestimates the surface Stokes drift in (f) despite the fact that the tail of the spectrum is slightly lower than that of WW3, which is consistent with the narrower directional spreading of the wind sea (Webb and Fox-Kemper, 2015). The approximation u_{sa} does a good job matching the broadband computations near the surface and at depth, but with larger differences at intermediate depths ($-1 > z > -10$), particularly in Fig. 4e.

Thus far we have focused on the profiles of the Stokes drift magnitude. The direction of a Stokes drift profile is constant with depth only when the directional wave spectrum is symmetric in azimuth and aligned in a particular direction across frequencies, which is often not the case for realistic spectra due to misalignment of the longer dominant waves and the wind or mixed wind-sea and swell (Sullivan et al., 2012; Lenain and Melville, 2014; Large et al., 2019; Romero

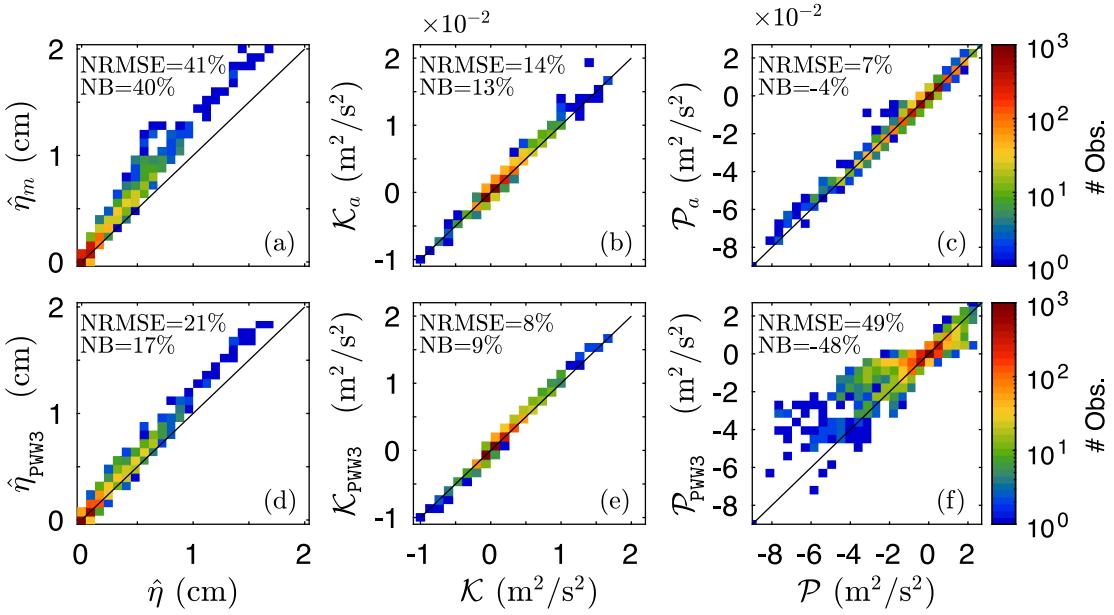

Fig. 7. Scatter plots comparing approximations (top) and the spectral reconstruction (bottom) against direct broadband computations for $\hat{\eta}_m$ (a, d), $\mathcal{K}_a$ (b, e), and $\mathcal{P}_a$ (c, f) computed offline at buoy locations with the WW3 and ROMS data from RHM20 month of December 2006 and Spring 2007.

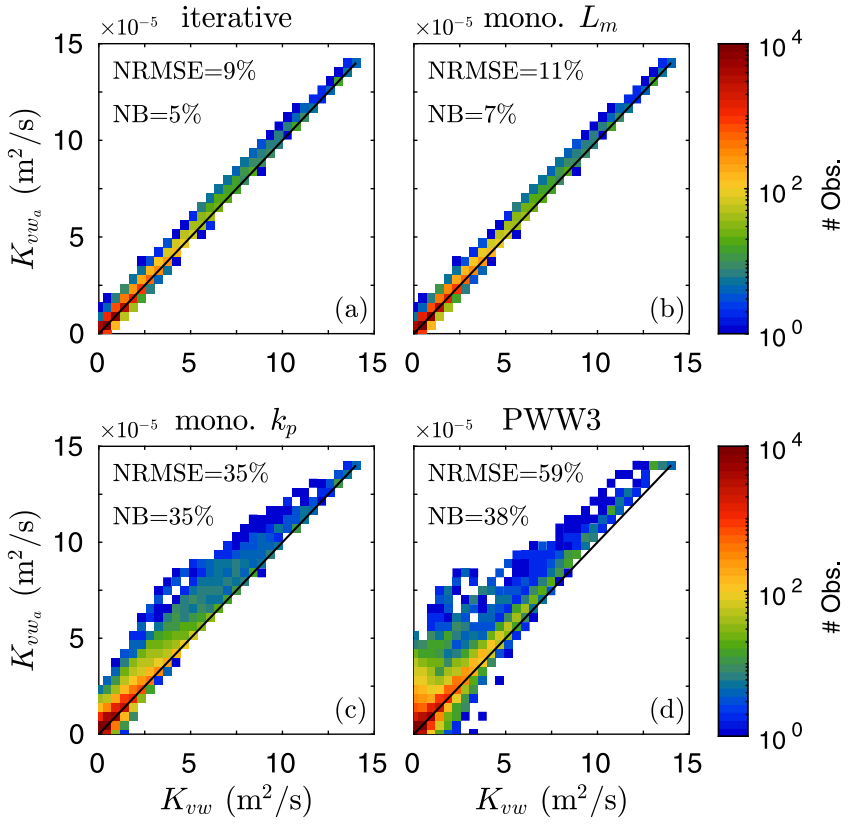

Fig. 8. Scatter plots comparing approximations against broadband computations for the three different approximations of K_{vw}: iterative (a), monochromatic based on L_m (b), and monochromatic based on k_p (c), and the spectral reconstruction (PWW3). Data are shown for depths between the surface and 60 m depth or the bottom, and were computed offline with the WW3 and ROMS data from RHM20 month of December 2006 and Spring 2007.

et al., 2019). Fig. 5 shows the vertical profiles of the Stokes drift direction θ_s for the examples shown in Figs. 3 and 4. The WW3 Stokes drift profiles (pink) of the large wave event (Figs. 5a, b) show angle variations of about 10 to 15 degrees between the surface and z=-20 m, which correlate with the approximation $\boldsymbol{u}_{sa}$ but with appreciable differences. The direction of $\boldsymbol{u}_{sa}$ smoothly connects the angles in depth of its constituents $\boldsymbol{u}_{se}$ and $\boldsymbol{u}_p$. In contrast, θ_s for the spectral reconstruction is depth independent because the spectrum only has a single peak leading to larger directional errors near the surface. For the case of mixed wind-sea and swell the spectral reconstruction gives excellent agreement with the full broadband profile $\theta_s(z)$, while that of the approximation $\boldsymbol{u}_{sa}$ gives similar trends compared to WW3 but

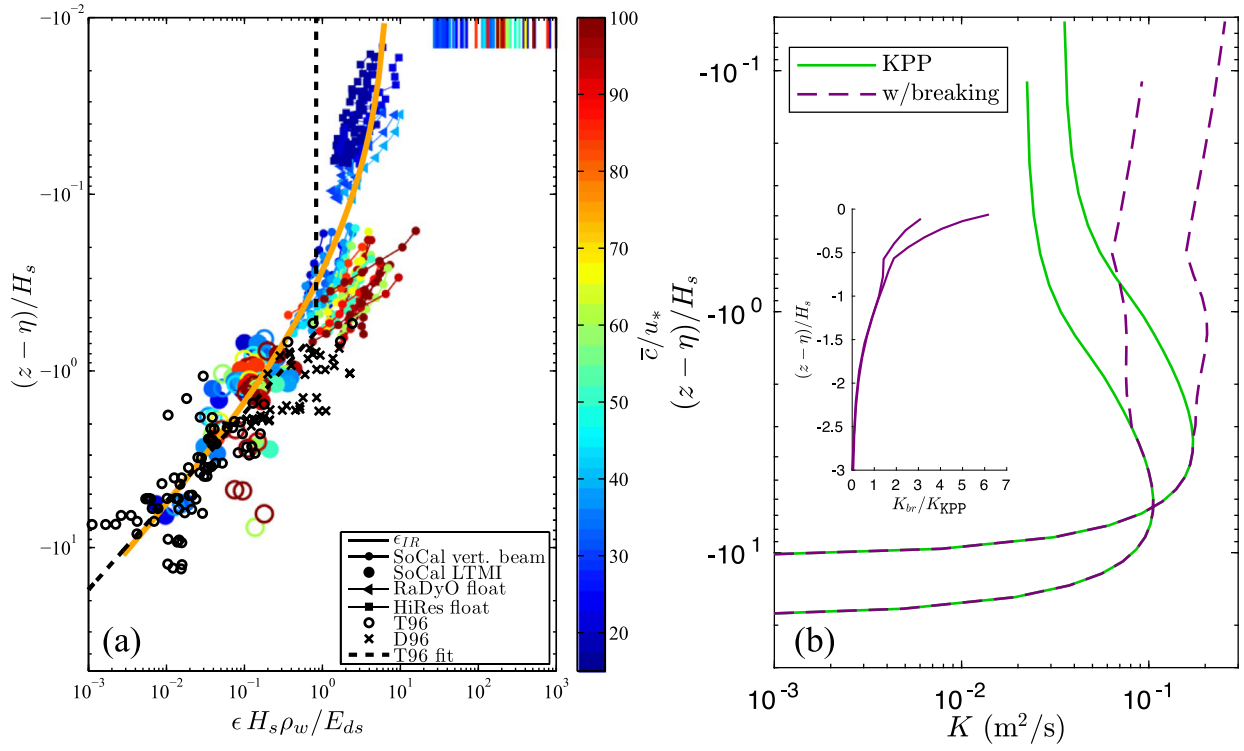

Fig. 9. (a) Turbulent kinetic energy dissipation scaled by H_s and the wave breaking energy dissipation E_{ds}. Figure from Sutherland and Melville (2015), showing their measurements color coded by wave age ($\bar{c}/u_*$) along with the data by Terray et al. (1996) and Drennan et al. (1996), u_* is the air-side friction velocity, and $\bar{c}$ is the spectrally weighted phase speed. Note that the data by Terray et al. (1996) and Drennan et al. (1996) were scaled by the wind input instead of the wavebreaking dissipation E_{ds}. The orange line shows the analytical profile in Eq. (45). (b) Sample vertical eddy viscosity profiles with near surface enhancement due to wave breaking (dashed purple — Eq. (46)) and without (KPP — green). The examples shown are for wind speeds of 13 and 19 m/s, H_s = 8.5 and 4.5 m, and E_{ds} = 1.9 and 0.55 W/m^2. The inset shows the corresponding K_{br} profiles normalized by KPP.

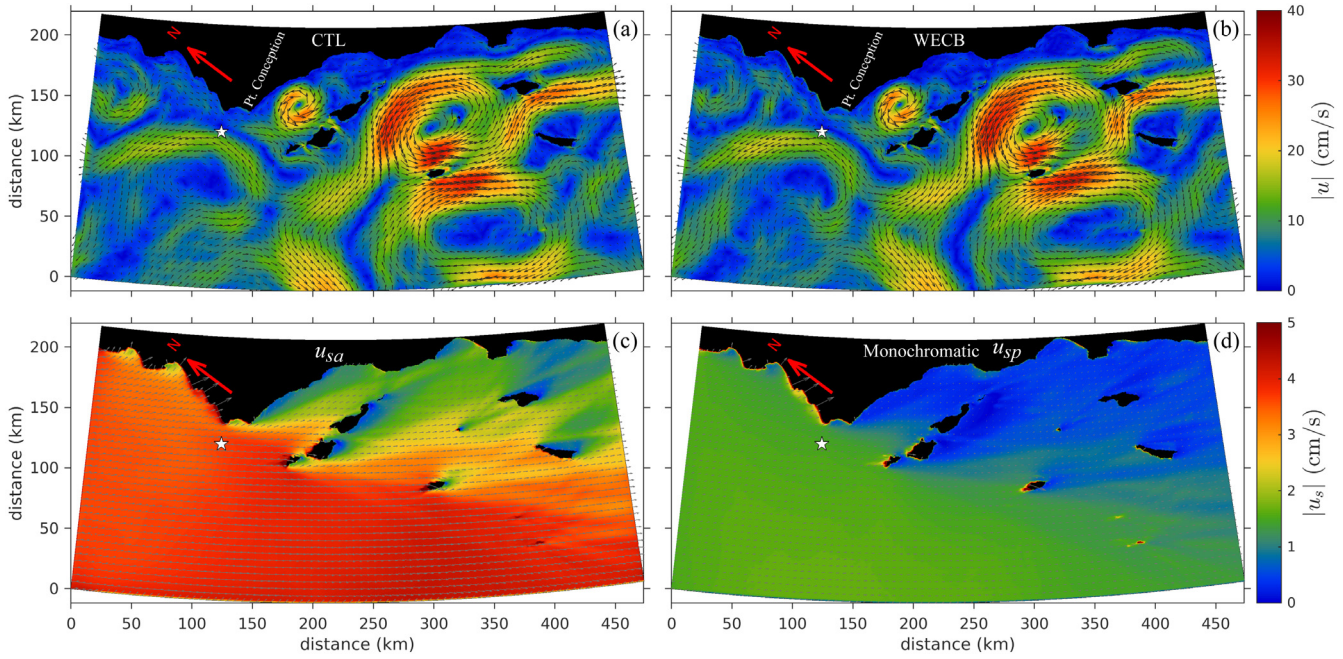

Fig. 10. Monthly average circulation at 1 m below the surface ($z = -1$ m) in Dec. 2006 with a horizontal resolution of 270 m for (a) the control run without wave forcing and (b) with broadband WEC forcing (WECB). The corresponding average Stokes drift ($\boldsymbol{u}_{sa}$) is shown in (c). The average spectral peak monochromatic Stokes drift ($\boldsymbol{u}_{sp}$) is shown in (d). The white star shows the location of the Harvest buoy.

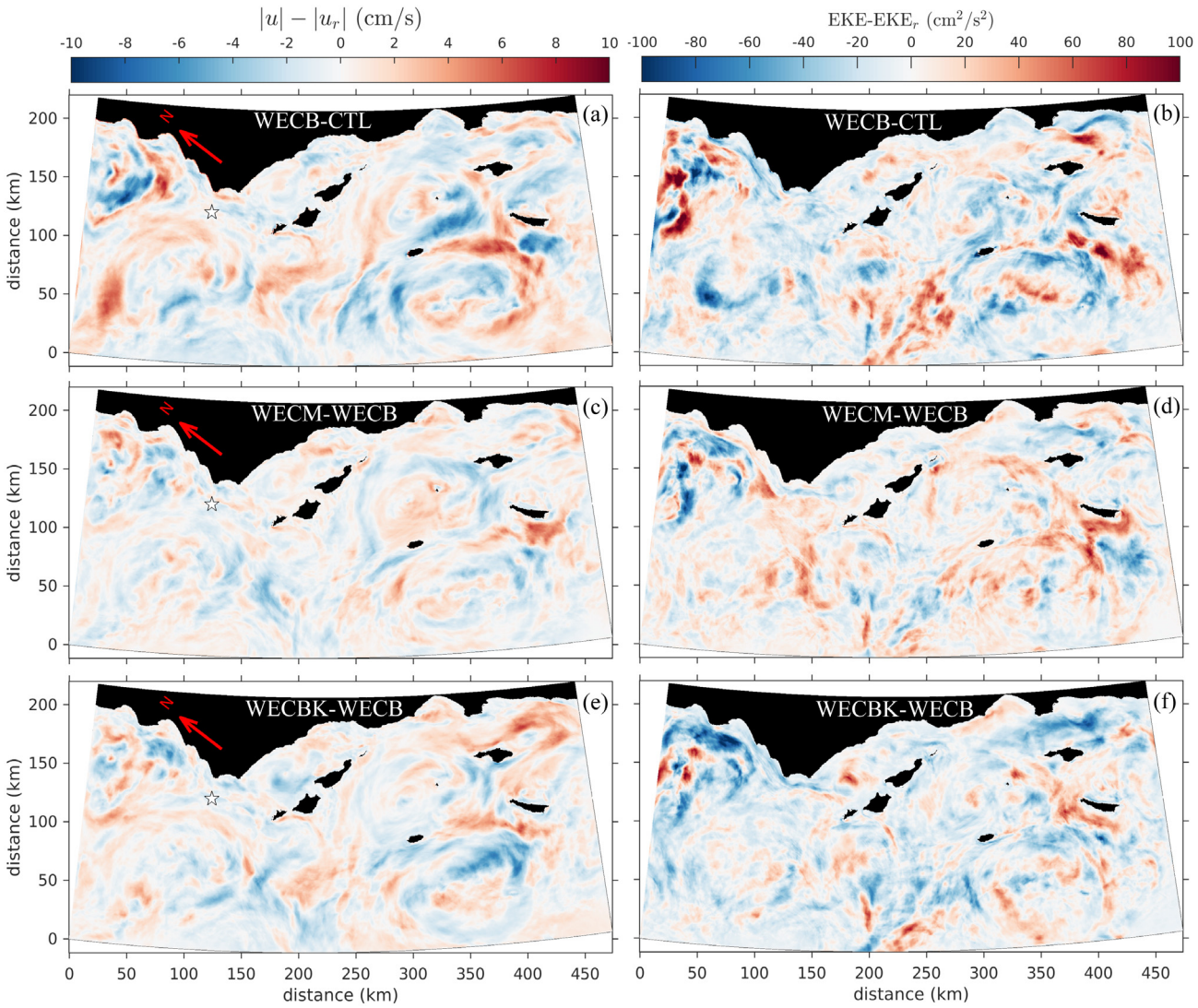

Fig. 11. Surface (z = −1 m) current magnitude and EKE differences between: (a, b) broadband WEC (WECB) and the control (CTL), (c, d) spectral peak monochromatic WEC (WECM) and WECB, and (e, f) WECB with near-surface vertical mixing due to breaking (WECBK) and WECB.

with finite errors. The directional error of the approximation at depth is directly dependent on how well the longer waves are aligned with the spectrally weighted mean direction $\overline{\theta}$. This can be improved for mixed wind-sea/swell conditions by using a mean wave direction weighted more strongly by the longer waves, or alternatively by using the mean swell direction from the partition PWW3 instead of $\overline{\theta}$ as shown in Figs. 5 with dotted purple lines.

The Stokes drift approximation was examined more thoroughly with the WW3 solutions from the two one-month-long periods, in December 2006 and the Spring 2007 (RHM20). The available wave spectra from the seven locations were used for this analysis. Bulk comparisons of the Stokes drift magnitude between the approximation (u_{sa}) and the spectral reconstruction (PWW3) against the broadband computations are shown in Figs. 6a, d, respectively. The data for all depths ($z > \max[-30, -h]$) are included. There is considerably more scatter in the spectral reconstruction compared to the approximation (u_{sa}). The normalized root-mean-square error (NRMSE) and the normalized bias (NB) defined as:

$$\mathrm{NB}(X) = \frac{\sum X - X_{ref}}{\sum X_{ref}} \tag{56}$$

and

$$\mathrm{NRMSE}(X) = \left(\frac{\sum (X - X_{ref})^2}{\sum X_{ref}^2} \right)^{1/2}, \tag{57}$$

where X is a given variable with known reference value X_{ref} (Ardhuin et al., 2010), are indicated in each panel. The Stokes drift approximation gives a NRMSE of 9% and no bias, whereas for the spectral reconstruction NRMSE = 26% and NB = −1%. These comparisons are dominated by the Stokes drift near the surface where the magnitude is largest. The same comparisons for cases without background swell shown in Figs. 6g, j give smaller errors by a 2% except for the bias of spectral reconstruction increasing in magnitude with NB = −4%.

The vertical distribution of the absolute magnitude differences of the Stokes drift approximation and the spectral reconstruction against (PWW3) against the spectral calculation are shown in Figs. 6b, e, respectively. The Stokes drift approximation shows the largest amplitude errors at about 2 m below the surface. In contrast, the spectral reconstruction gives the largest errors near the surface, spanning a much wider range than that of the approximation, which is consistent with the scatter shown in 6a, d. However, the vertical profile of angle deviations from the spectral calculation are on average larger for the Stokes drift approximation compared to the spectral reconstruction shown in Figs. 6c, f. The average RMS angle deviations are 6 ° and 3 °

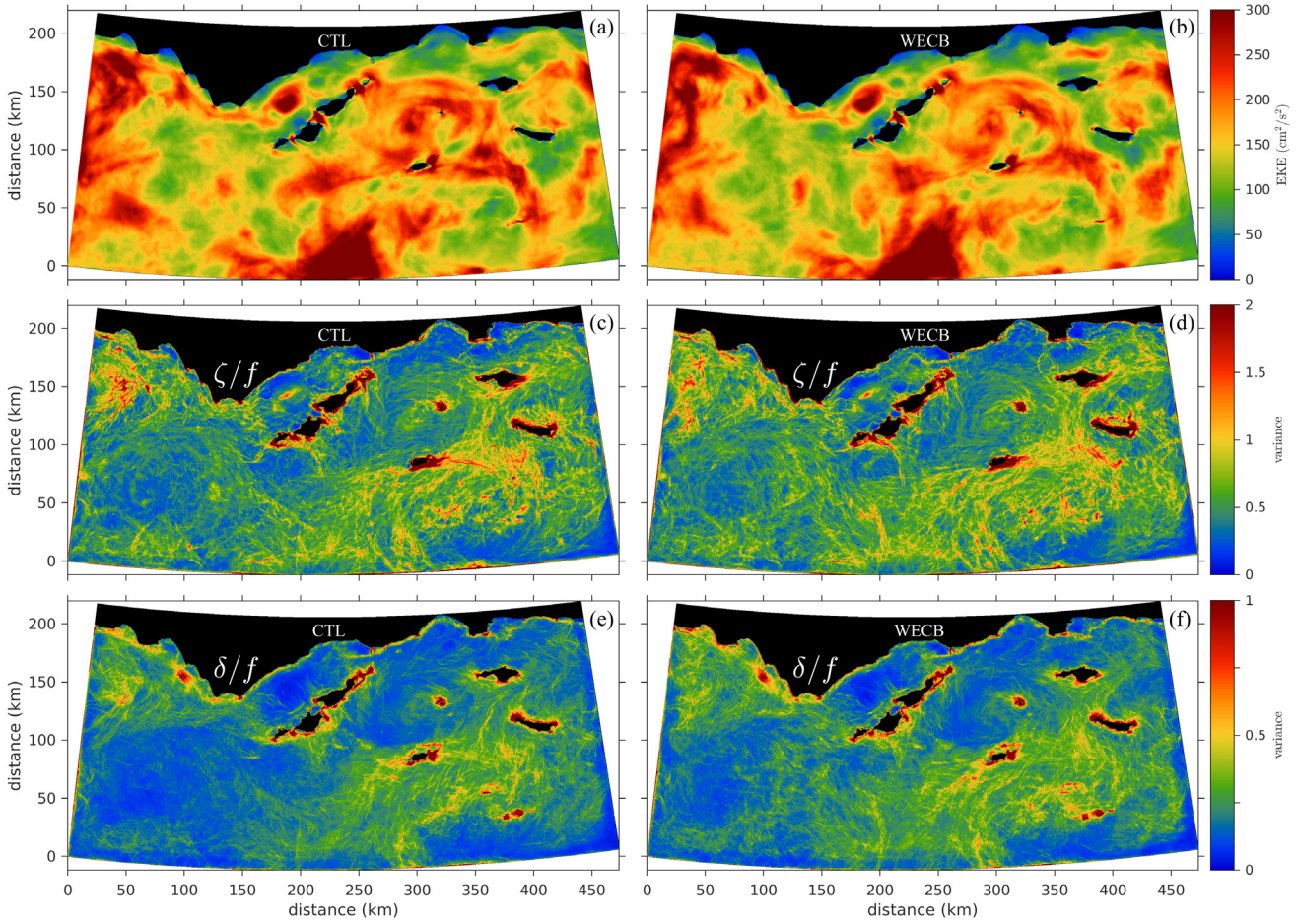

Fig. 12. Monthly eddy kinetic energy (EKE), and relative vorticity ζ/f and divergence δ/f variance at 1 m below the surface ($z = -1$ m) for Dec. 2006 with a horizontal resolution of 270 m. The control (CTL) run without wave forcing is in (a–c) and the WEC run in (d–f).

for u_{sa} and PWW3, respectively, which are indicated with dashed lines (Fig. 6e, f). Excluding the cases with background swell, the vertical errors of the Stokes drift approximation are slightly reduced for the amplitude and significantly reduced for the direction without several outliers (Figs. 6h, i). The vertical distribution of the Stokes drift error for the spectral reconstruction without background swell (Fig. 6k, l) is nearly unchanged for the magnitude and only slightly improved for the direction near the surface.

This analysis shows that neither method is perfect but the method here described captures most of the variability of the Stokes drift. The spectral reconstruction does best in terms of directionality at depth for mixed wind-sea/swell conditions. Near the surface where most of the Stokes drift is contained, the errors of the spectral reconstruction can be substantial in both magnitude and direction. As shown earlier, the directional error of Stokes drift approximation in the presence of a background swell can be reduced by using the swell direction, when available.

3.2. Set-down, Bernoulli head, and quasi-static pressure

The set-down comparing the monochromatic and the spectral reconstruction estimates (PWW3) against direct computations from the resolved spectra are plotted in 7a, d, respectively. Both the NB and NRMSE are about 40% for the monochromatic values and 20% for the spectral reconstruction. Our WEC implementation with ROMS uses $\hat{\eta}$ from WW3. The ratio $\hat{\eta}_m/\hat{\eta}$ is used for the computation of $\mathcal{P}_a$. The set-down for the data here analyzed is negligible except for the cases in relatively shallower water ($h = 20$ m). The corresponding Bernoulli head and pressure approximations evaluated offline against direct computations from resolved spectra are shown in Figs. 7b, c. There is a good correspondence between the two sets with NB of 13% and -4%, and NRMSE of 14% and 7%, for $\mathcal{K}_a$ and $\mathcal{P}_a$, respectively. The spectral reconstruction (Fig. 7e, f) gives slightly smaller errors for the Bernoulli head and much larger errors for the quasi-static errors of about 50% for both NRMSE and NB.

3.3. Vertical mixing due to non-breaking unsteady waves

We proceed to analyze the different approximations of the wave-induced vertical diffusivity due to unsteady waves (26). Fig. 8a–c shows a scatter plot comparing the approximations to the direct estimates of K_{vw} from the directional spectrum. The iterative method, monochromatic based on mean wavelength L_m, and monochromatic based on the peak wavenumber are shown in panels (a–c), respectively. The iterative method gives the smallest errors with NRMSE = 9% and a small positive bias NB = 5%, both of which increase to NRMSE = 11% and NB = 7% for the method based on L_m. The approximation in terms of k_p gives the largest errors with NRMSE = NB = 35%. In practice, the iterative method would require the depth-integrated vertical parcel displacement R^2_{vw} (Eq. (29)), which is not a standard output parameter of WW3. However, L_m is an optional output parameter of WW3 and can be used to approximate K_{vw} along with H_s with relatively small errors. Alternatively, H_s and k_p can be used to approximate K_{vw} but with substantial errors. The corresponding values calculated from the spectral reconstruction gives much larger errors (Fig. 8d) with NRMS=59% and a positive normalized bias of 38%.

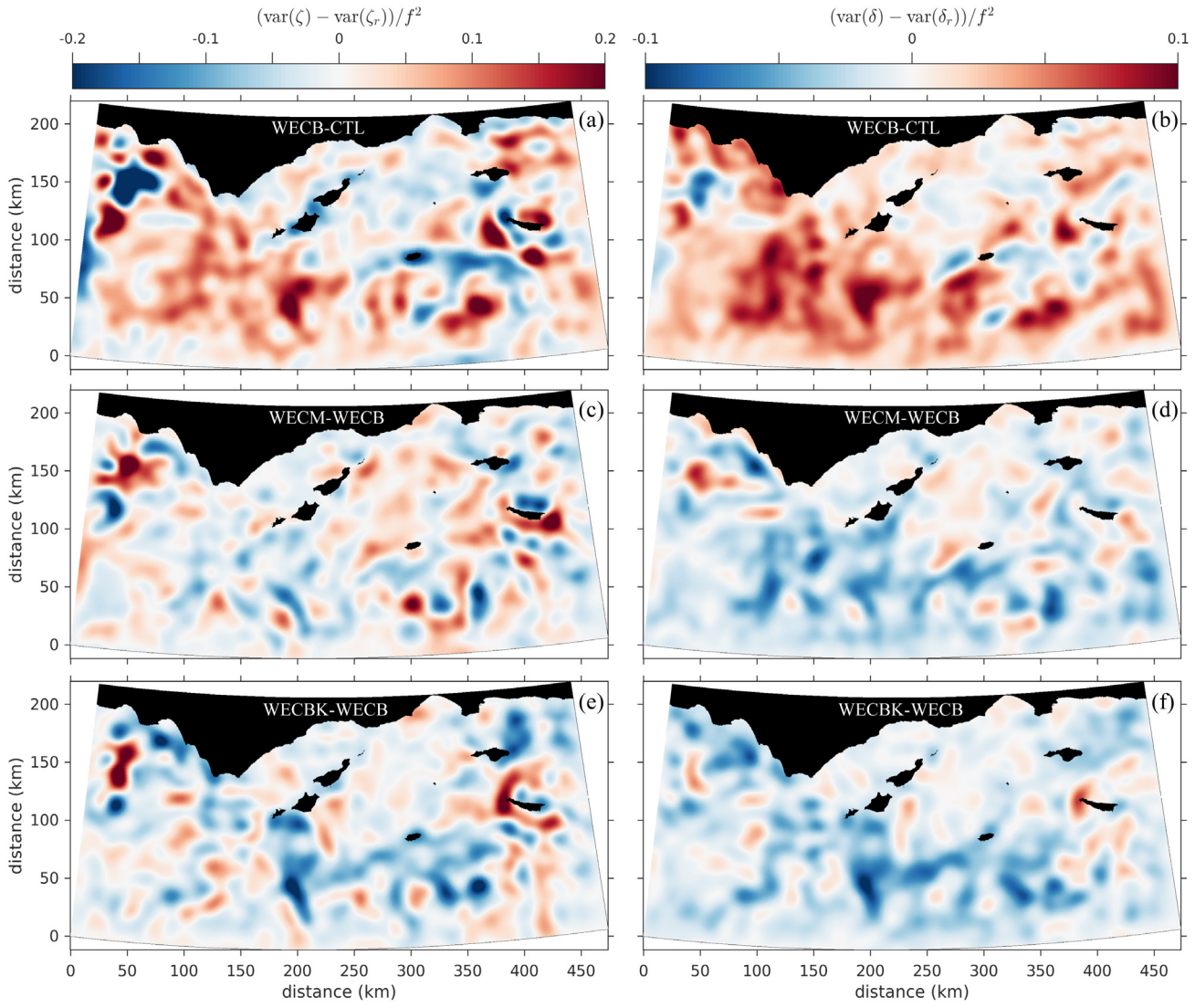

Fig. 13. Filtered vorticity (a) and divergence (b) monthly variance differences between the WEC and control solutions, respectively. The corresponding differences between WEC runs for WECM-WECB and WECBK-WECB are shown in (c, d) and (e, f), respectively. The vorticity and divergence were calculated at 1 below the surface. The variances were smoothed with an isotropic 20 km low-pass filter.

3.4. Vertical mixing due to wave breaking

Here we demonstrate the parameterization of the vertical mixing due to wave breaking. The non-dimensional TKE dissipation profile (45) is plotted on the figure of SM15 in Fig. 9a. The SM15 data, color-coded by wave age, includes near-surface measurements obtained with an infrared stereo camera system. Our profile approximately matches the measurements at lower wave ages and does not account for the large dissipation values closest to the surface. The large dissipation values are confined to a thin layer with a small contribution to the depth-integrated dissipation. Fig. 9b shows two examples of the vertical mixing with and without the contribution due to wave breaking. The two cases shown are in deep-water with conditions with wind speeds of 13 and 19 m/s, $H_s = 8.5$ and 4.5 m, and $E_{ds} = 1.9$ and 0.55 W/m^2, with the stronger forcing case corresponding the profile with larger vertical mixing. The contribution of K_{br} closest to the surface 2–6 for times the magnitude of KPP for these examples as shown in the inset.

3.5. Wave effects on currents

In this subsection, one-month-long ROMS solutions for the regional configuration are analyzed in terms of the mean circulation, eddy kinetic energy, and current gradients. The purpose of this analysis is to highlight some of the impacts of due to WEC. We compare different WEC solutions against one another and the control without WEC. A detailed analysis of WEC at submesoscales in the open ocean is described in Hypolite et al. 2021.

The average circulation at 1 m below the surface for the month of December 2006 is shown in Fig. 10a, b, corresponding to the control (CTL) and broadband WEC (WECB) solution, respectively. The corresponding monthly average Stokes drift velocity at $z = -1$ m is mapped in Fig. 10c, reaching a magnitude of 5 cm/s due to the Southeast in the open ocean. This is consistent with the predominant wind forcing from the Northwest. There is an obvious contrast for the surface Stokes drift in the open ocean compared the Southern California Bight, which is sheltered by the abrupt change of the coastline at Point Conception and the islands. Therefore WEC is expected to be most significant outside the Bight from increased exposure to wave forcing.

The monthly circulation of the control and the WEC solution are very similar both in the open ocean and sheltered areas, with a few noticeable differences (Fig. 11a). The largest differences are primarily due horizontal mismatch of the mesoscale mean circulation, which can be seen in patterns with alternating sign surrounding the mesoscale flow. North of point conception there is an increase of the mean

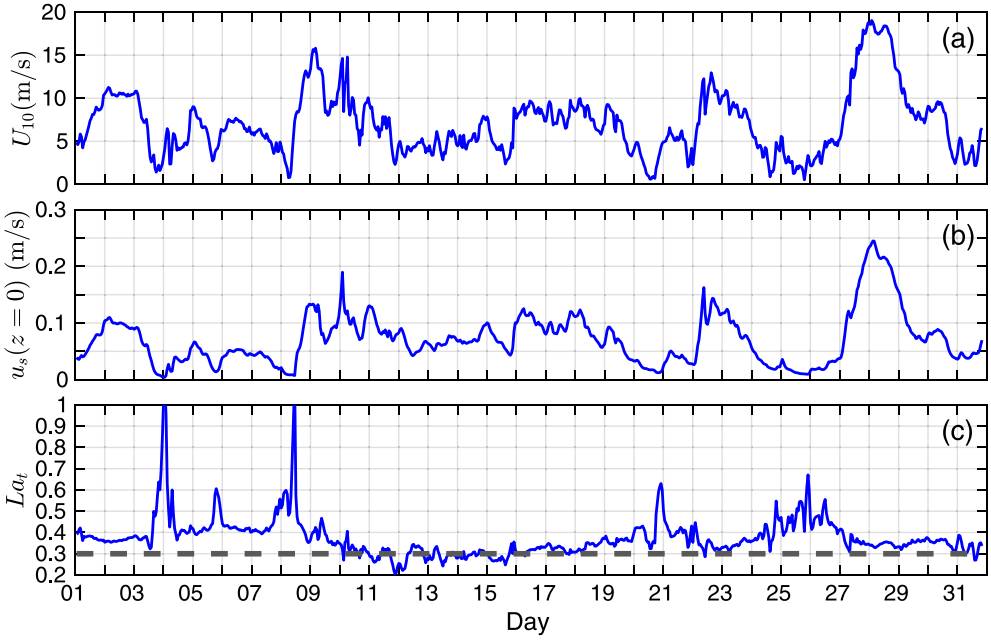

Fig. 14. Time series of surface wind speed (a), resolved surface Stokes drift (b), and Turbulent Langmuir number (c) at Harvest (see Fig. 10) during the month of December 2006.

circulation along the perimeter of the coast and a reduction of the mean current further offshore over areas exposed to the incoming wave energy. The mean circulation from the other solutions (WECM and WECBK) are also very similar and therefore are not shown. For reference, the average spectral peak monochromatic Stokes drift at $z = -1$ m is shown in Fig. 10d being about half of the broadband mean in open ocean (Fig. 10c). The difference in mean current magnitude for WECM and WECBK relative to WECB are shown in Fig. 11c, e. Again the differences primarily show structural differences around the mesoscale circulation. The mean circulation for WECM is more similar to WECB compared to WECBK, which shows largest differences. The WECBK solution gives a reduction of the current amplitude over the Santa Barbara Eddy (i.e., the cyclonic circulation within the Santa Barbara Channel). Suggesting that vertical shear is important for the eddy.

The eddy kinetic energy EKE defined as EKE $= \frac{1}{2}[\langle u'^2\rangle + \langle v'^2\rangle]$, with $\mathbf{u}' = \mathbf{u} - \langle \mathbf{u}\rangle$ corresponding to the current anomaly and the brackets denoting the temporal monthly average, is shown at 1 m below the surface for CTL and WECB in Figs. 12a, b. Overall, the large-scale EKE pattern is again very similar between the two runs with minor qualitative differences. Differences in EKE between WECB and CTL in Fig. 11b are primarily due to the misalignment of the large-scale circulation. There is a coherent reduction in EKE due to WEC along the coast north of Point Conception in the Santa Maria Basin. The monochromatic WEC forcing compared to WECB gives on average increased surface EKE (11d). In contrast, the vertical diffusivity due to breaking on average reduces the near surface EKE (11e). This shows that WEC forcing here considered has relatively small impacts on the mean circulation and the mesoscale current variability the ocean surface for the relatively short model integration of one month with tightly nudged boundaries toward the parent solution.

We further explore the impacts of WEC on small-scale current variability starting with monthly variances of the vorticity ($\zeta = v_x - u_y$) and divergence ($\delta = u_x + v_y$) also computed at 1 m below the surface for CTL and WECB (Figs. 12c–f). The vorticity variance is larger than that of the divergence by about a factor of 2 for both WEC and the control solution. Both the vorticity and divergence variances are enhanced in the open ocean by WEC compared to the control. The increase of the variances is most evident in the lower-left area of the model configuration. To better assess the WEC impacts, the variance fields were smoothed with a 20 km isotropic low-pass filter and directly compared through the differences (WEC minus the control) which are shown in Figs. 13a, b, corresponding to the vorticity and divergence fields, respectively. WEC on average increases the vorticity and divergence variances, particularly in the open ocean with increased exposure to wave forcing. However, these effects are partially reduced for the spectral peak monochromatic WEC forcing 13c, d or when the vertical mixing due to wave breaking is included 13e, f, in particular for the surface divergence.

The WEC effects on the surface current variability are further analyzed with respect to the Turbulent Langmuir Number $La_t = \sqrt{u_*^w/u_s(0)}$, which was introduced by McWilliams et al. (1997) to characterize Langmuir turbulence of Large Eddy Simulations (LES) with u_*^w corresponding to the water-side friction velocity. Our ROMS solutions are hydrostatic and larger scale, yet it is reasonable to expect that the impacts of WEC can be characterized to some extent with La_t. As a starting point, we consider the time series of wind speed, resolved surface stokes drift and La_t at Harvest in the open ocean (Fig. 14). The location of the Harvest buoy is indicated with a white start in Fig. 10. There are three events with wind speeds exceeding 15 m/s and resolved surface Stokes drift exceeding 15 cm/s, with the largest wind/wave event toward the end of the month. La_t varies between 0.2 and 1, but generally asymptotes toward 0.3, which is representative of the Langmuir Turbulence regime (McWilliams et al., 1997). The lowest values of La_t happen between storms when the wind speed is small and the Stokes drift is relatively large. During the three large wind events, La_t approaches 0.3 but generally remains just above it.

Taking the time series at Harvest as representative of the synoptic wave forcing conditions, we sorted the model data into two groups to compute ensemble statistics: a strong wave forcing group with $La_t < 0.37$ (La_{t_1}), and a weak wave forcing group with $La_t > 0.37$ (La_{t_2}). The threshold of 0.37 is arbitrary but small changes to the threshold do not affect the results of the analysis. The resulting maps for the average La_t are shown in Fig. 15a, b. In the open ocean $\langle La_t\rangle$ is about 0.33 and 0.43 for the strong (La_{t_1}), and weak (La_{t_1}) wave forcing cases, respectively. The corresponding filtered vorticity and divergence variance differences between WECB and non-WEC are shown in panels c, d and e, f, respectively. The vorticity and divergence variances due to WEC are largest for the group with the lower La_t in the open ocean. In

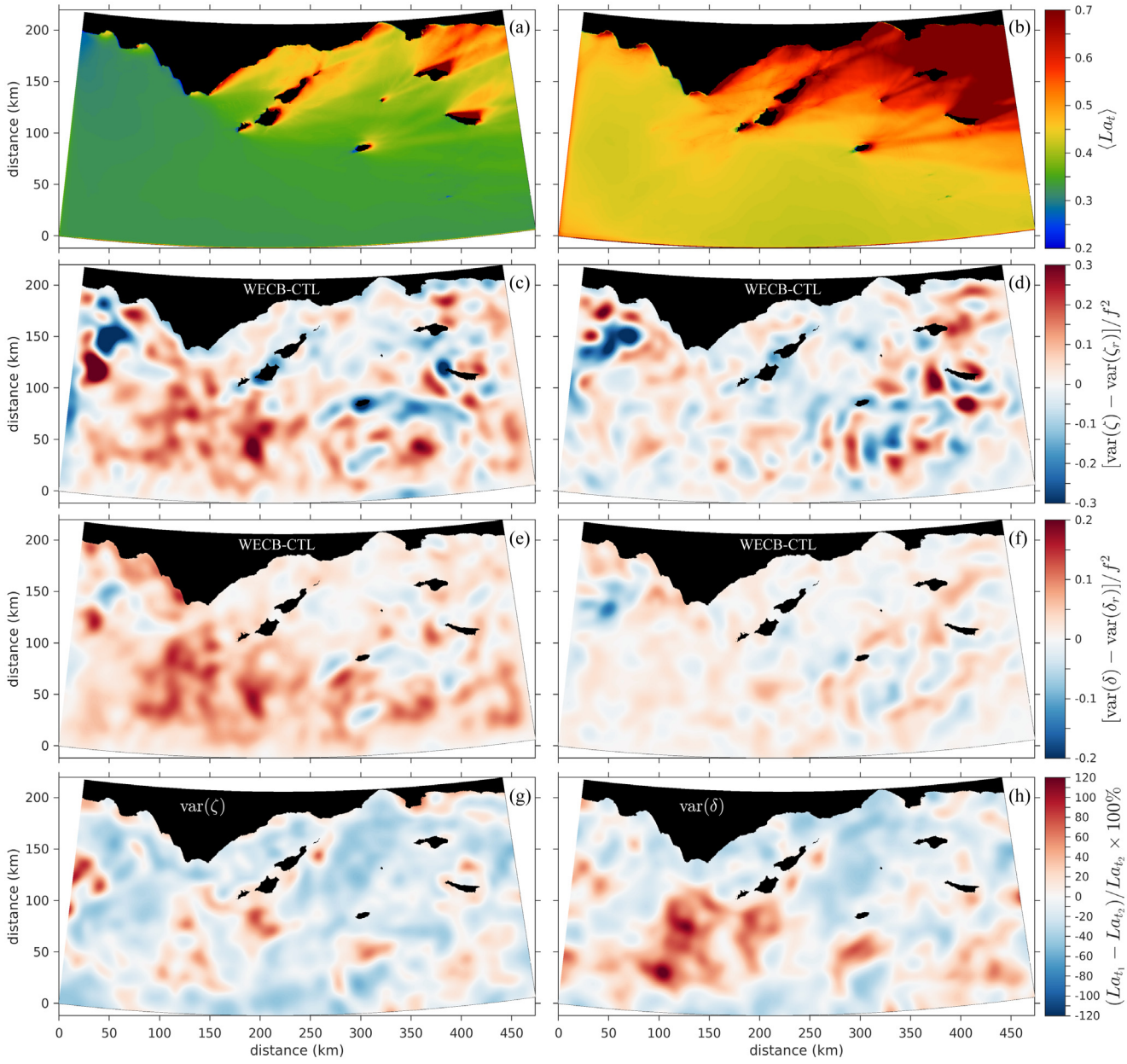

Fig. 15. Filtered vorticity and divergence variance differences between the WEC and control solutions as in Fig. 13 for periods with different forcing conditions based on a La_t threshold of 0.37 in the open ocean at Harvest (Fig. 14). The average La_t maps for the two ensembles are shown in (a, La_{t_1}) and (b, La_{t_2}) with mean values in the open ocean of about 0.33 and 0.43, respectively. The corresponding maps of filtered vorticity and divergence monthly variance differences between WECB and the control solution are shown in (c, d) and (e, f), respectively. The relative differences between the two groups plotted as percentage are shown in (g) and (h) for the vorticity and divergence variances, respectively.

contrast, the impacts of WEC on the vorticity and divergence variances within the Southern California Bight are generally small where La_t is large. The relative variance differences between the two groups for WECB (Figs. 15g, h) show no bias for the vorticity and a positive bias for the divergence with values of up to +120% corresponding to larger divergence variance for the group with larger wave forcing (La_{t1}). This shows that although the current gradient variability differences relative to the control are inversely related to La_t, the current gradient variability for the WECB run at low La_t is increased only for the divergence offshore.

The work by Hypolite et al. (2021) investigates WEC in the open ocean at submesoscales in more detail, including higher horizontal resolution, comparing conditions with remotely generated swell vs locally forced wind waves. Their analysis shows that WEC impacts increase with increasing model resolution. They also show that WEC enhances the near-surface velocity and density gradients, but locally generated waves additionally result in a sink of surface buoyancy gradients from the onset of small-scale structures with strong current gradients and vertical velocities.

4. Summary and discussion

We presented a set of wave approximations and a parameterization of the vertical mixing due to wave breaking for coupled wave–ocean models within the wave-average framework by McWilliams et al. (2004). The proposed framework is well suited for coastal applications, not limited to deep-water or narrowband waves, and is significantly

more efficient, and accurate to a certain extent, than the spectral reconstruction approach proposed by Kumar et al. (2017). The approximations were demonstrated offline with solutions from WW3 for an idealized shoaling wave spectrum and validated with model data from a realistic regional model configuration in Southern California. The approximation of the Stokes drift uses a two-scale approach to handle misaligned winds and dominant waves and mixed wind-sea and swell conditions. The Stokes drift approximation gives overall smaller errors in magnitude with NRMSE = 9% compared to the spectral reconstruction of Kumar et al. (2017) based on a JONSWAP spectrum with NRMSE of 26%. In terms of direction, the proposed approximation gives smaller errors near the surface but larger errors at depth compared to the spectral reconstruction, especially in conditions with mixed wind-sea and swell. The Bernoulli head approximated monochromatically using the spectral peak information (UMS10) and the spectral reconstruction was shown to give errors of about 14% and 8%, respectively. The quasi-static pressure based on a two-scale approach resulted in NRMSE of 7% and a bias of −4%, whereas the spectral reconstruction gives much larger errors approaching 50%. Approximations of the wave-induced vertical diffusivity due to the time-rate of change of particle displacement square resulted in errors of 11% or smaller, increasing to 35% for the monochromatic approximation based on the spectral peak information and larger errors (59%) for the spectral reconstruction.

We implemented the wave approximations and vertical mixing parameterization due to breaking in ROMS building on the work by UMS10. The wave parameters used for the conservative ROMS WEC forcing files are A_w, peak wave period T_p, $\bar{\theta}$, surface and depth-average Stokes drift vector, and set-down adding to a total 8 parameters which is exactly twice the number of parameters used by the original code of UMS10 for non-conservative WEC forcing. A similar number of parameters is needed for a spectral reconstruction and two spectral bands (wind-sea and swell). A total of 8 parameters is relatively small compared to 500 or more for a full spectral coupling, depending on the resolution of the directional spectrum of the wave model. In terms of computation our WEC implementation is slower than the original code of UMS10 by about 20%. This a relatively small additional cost when compared to the spectral reconstruction approach or a full 2d spectrum exchange from the wave model for which the WEC terms have to be computed for all spectral components and added together, effectively increasing the number of operations by a factor NF×ND, with NF and ND corresponding to the number of frequencies and directions used to discretize the wave spectrum in ROMS. To compute the WEC terms spectrally with a 15 degree resolution (ND = 24) and 20 frequencies the cost would increase by a factor of 500, which is prohibitive at the moment for realistic applications.

The new WEC framework was tested with a regional configuration forced offline with WW3. A one-month-long solution in Southern California with a horizontal resolution of 270 m was compared against a control solution without wave forcing. WEC impacts on the monthly average near-surface circulation and eddy kinetic energy are small. WEC impacts are most significant at small scales increasing surface current gradient variability, with larger impacts when the Turbulent Langmuir number is small. The surface current gradient variability enhancement due to WEC near the surface is partially reduced when the vertical mixing due breaking is included. Similarly, WEC impacts on surface current variability are larger for broadband WEC forcing compared to the spectral peak monochromatic approach.

The proposed wave approximations improve upon the work by UMS10 by accounting for finite spectral bandwidth, not limited to only using the spectral peak information. This allows for the modeling of wave effects on currents more realistically including conditions of mixed wind-sea and swell. The Stokes drift approximation makes no assumption about the spectral shape, unlike other studies that impose or assume a spectral shape (e.g., Breivik et al., 2014; Kumar et al., 2017). The proposed approximation is the only one to this day that is both performant and realistic for broadband spectra. Ultimately, WEC forcing ideally should be computed directly from the directional wave spectrum at the expense of significantly increasing the amount of information exchanged across models and computation, but is not feasible for realistic configurations. The current approach allows for the investigation of wave–current interactions seamlessly across the open ocean, continental shelf, inner-shelf and surf zone. Future applications include investigation of WEC on material transport and dispersion (e.g., Romero et al., 2013, 2016) , including cross-shelf and air–sea exchange.

CRediT authorship contribution statement

Leonel Romero: Conceptualization, Methodology, Software, Validation, Formal analysis, Visualization, Investigation, Writing – original draft. **Delphine Hypolite:** Conceptualization, Methodology, Software, Writing – review & editing. **James C. McWilliams:** Conceptualization, Writing – review & editing.

Declaration of competing interest

The authors declare that they have no known competing financial interests or personal relationships that could have appeared to influence the work reported in this paper.

Acknowledgments

We thank Yusuke Uchiyama for useful discussions. We appreciate the comments from anonymous reviewers which lead to substantial improvements of the manuscript. This work used computing resources from DoD HPC Modernization Program, NCAR's Computational and Information Systems Lab (CISL), and Extreme Science and Engineering Discovery Environment (XSEDE) #TG-OCE030000N. LR was supported by ONR, United States N00014-16-1-2936 and the National Science Foundation (NSF), United States OCE-1924686. JCM and DH acknowledge support from Calif. Natural Resources Agency, United States C0100400, NOAA, United States 0471-2015:04, NSF OCE-1355970, and ONR, United States N00014-15-1-2645.

References

Agrawal, Y.C., Terray, E.A., Donelan, M.A., Hwang, P.A., Williams, A.J., Drennan, W.M., Kahma, K.K., Krtaigorodskii, S.A., 1992. Enhanced dissipation of kinetic energy beneath surface waves. Nature 359, 219–220.

Ardhuin, F., O'Reilly, W.C., Herbers, T.H., Jessen, P.F., 2003. Swell transformation across the continental shelf. Part I: Attenuation and directional broadening. J. Phys. Oceanogr. 33, 1921–1939.

Ardhuin, F., Rogers, E., Babanin, A.V., Filipot, J.-F., Magne, R., Roland, A., van der Westhuysen, A., Queffeulou, P., Lefevre, J.-M., Aouf, L., Collard, F., 2010. Semiempirical dissipation source functions for ocean waves. Part I: Definition, calibration, and validation. J. Phys. Oceanogr. 40, 1917–1941.

Battjes, J.A., Janssen, J.P.F.M., 1978. Energy loss and set-up due to breaking of random waves. In: 16th International Conference on Coastal Engineering. Hamburg, Germany, pp. 569–588.

Booij, N., Ris, R.C., Holthuijsen, L.H., 1999. A third-generation wave model for coastal regions 1. Model description and validation. J. Geophys. Res. 104, 7649–7666.

Breivik, Ø., Christensen, K.H., 2020. A combined stokes drift profile under swell and wind sea. J. Phys. Oceanogr. 50, 2819–2833.

Breivik, Ø., Janssen, P.A.E.M., Bidlot, J.-R., 2014. Approximate Stokes drift profiles in deep water. J. Phys. Oceanogr. 44, 2433–2445.

Breivik, K., Bidlot, J.-R., Balmaseda, M.A., Janssen, P.A.E.M., 2015. Surface wave effects in the NEMO ocean model: Forced and coupled experiments. J. Geophys. Res. Ocean. 120, 2973–2992.

Burchard, H., 2001. Simulating the wave-enchanced layer under breaking surface waves with two-equation turbulence models. J. Phys. Oceanogr. 31, 3133–3145.

Chapman, D.C., 1985. Numerical treatment of cross-shelf open boundaries in a barotropic coastal ocean model. J. Phys. Oceanogr. 15, 1060–1075.

Craig, P.D., Banner, M.L., 1994. Modeling wave-enhanced turbulence in the ocean surface layer. J. Phys. Oceanogr. 24, 2546–2559.

Craik, A.D.D., Leibovich, S., 1976. A rational model for Langmuir circulations. J. Fluid Mech. 73, 401–426.

Dauhajre, D.P., McWilliams, J.C., Renault, L., 2019. Nearshore Lagrangian connectivity: Submesoscale influence and resolution sensitivity. J. Geophys. Res. Ocean. 124, 5180–5204.

Drennan, W.M., Donelan, M.A., Terray, E.A., Katsaros, K.B., 1996. Oceanic turbulence dissipation measurements in SWADE. J. Phys. Oceanogr. 26, 808–815.
Durski, S.M., Haidvogel, D.B., 2004. Vertical mixing schemes in the coastal ocean: Comparison of the level 2.5 Mellor–Yamada scheme with an enhanced version of the K profile parameterization. J. Geophys. Res. 109, C01015.
ECMWF, 2013. IFS Documentation CY38R1 - Part VII: ECMWF wave model. In: IFS Documentation CY38R1 Number 7 in IFS Documentation. ECMWF.
Esters, L., Breivik Landwehr, S., ten Doeschate, A., Sutherland, G., Christensen, K.H., Bidlot, J.R., Ward, B., 2018. Turbulence scaling comparisons in the ocean surface boundary layer. J. Geophys. Res. Ocean. 123, 2172–2191.
Flather, R.A., 1976. A tidal model of the north–west European continental shelf. Mem. Soc. R. Sci. Liege 6, 141–164.
Hanson, J.L., Phillips, O.M., 2001. Automated analysis of ocean surface directional wave spectra. J. Atmos. Ocean. Technol. 18, 277–293.
Hanson, J.L., Tracy, B.A., Tolman, H.L., Scott, R.D., 2009. Pacific Hindcast performance of three numerical wave models. J. Atmos. Ocean. Technol. 26, 1614–1633.
Hasselmann, K., 1970. Wave-driven inertial oscillations. Geophys. Fluid Dyn. 1, 463–502.
Hasselmann, S., Hasselmann, K., 1985. Computations and parameterizations of the nonlinear energy transfer in a gravity-wave specturm. Part II: Parameterizations of the nonlinear energy transfer for application in wave models. J. Phys. Oceanogr. 15, 1378–1391.
Herterich, K., Hasselmann, K., 1982. The horizontal diffusion of tracers by surface waves. J. Phys. Oceanogr. 12, 704–711.
Hypolite, D., Romero, L., McWilliams, J.C., Dauhajre, D.P., 2021. Surface gravity wave effects on submesoscale currents in the open ocean. J. Phys. Oceanogr. in press.
Janssen, P., 2012. Ocean wave effects on the daily cycle in SST. J. Geophys. Res. Ocean. 117, 1–24.
Kenyon, K.E., 1969. Stokes drift for random gravity waves. J. Geophys. Res. 2, 6991–6994.
Kumar, N., Cahl, D.L., Crosby, S.C., Voulgaris, G., 2017. Bulk versus spectral wave parameters: Implications on Stokes drift estimates, regional wave modeling, and HF radars applications. J. Phys. Oceanogr. 47, 1413–1431.
Kumar, N., Feddersen, F., Uchiyama, Y., McWilliams, J.C., O'Reilly, W.C., 2015. Mid-shelf to surf zone coupled ROMS-SWAN model-data comparison of waves, currents, and temperature : Diagnosis of subtidal forcings and response. J. Phys. Oceanogr. 45, 1464–1490.
Kumar, N., Voulgaris, G., List, J.H., Warner, J.C., 2013. Alongshore momentum balance analysis on a cuspate foreland. J. Geophys. Res. Ocean. 118, 5280–5295.
Kumar, N., Voulgaris, G., Warner, J.C., Olabarrieta, M., 2012. Implementation of the vortex force formalism in the coupled ocean-atmosphere-wave-sediment transport (COAWST) modeling system for inner shelf and surf zone applications. Ocean Model. 47, 65–95.
Large, W.G., 2006. Surface fluxes for practitioners of global ocean data assimilation. In: Chassignet, E.P., Verron, J. (Eds.), Ocean Weather and Forecasting. Springer, pp. 229–270.
Large, W.G., McWilliams, J.C., Doney, S.C., 1994. Oceanic vertical mixing: A review and a model with a nonlocal boundary layer parameterization. Rev. Geophys. 32, 363–403.
Large, W.G., Patton, E.G., DuVivier, A.K., Sullivan, P.P., Romero, L., 2019. Similarity theory in the surface layer of large-eddy simulations of the wind-, wave-, and buoyancy-forced Southern ocean. J. Phys. Oceanogr. 49, 2165–2187.
Large, W.G., Yeager, S.G., 2004. Diurnal to Decadal Global Forcing for Ocean and Sea–Ice Models: The Data Sets and Flux Climatologies. NCAR Tech. Note, TN–460+ST, 105pp.
Lenain, L., Melville, W.K., 2014. Autonomous surface vehicle measurements of the ocean's response to tropical cyclone freda. J. Atmos. Ocean. Technol. 31, 2169–2190.
Lenain, L., Melville, W.K., 2017. Measurements of the directional spectrum across the equilibrium saturation ranges of wind-generated surface waves. J. Phys. Oceanogr. 47, 2123–2138.
Lenain, L., Pizzo, N., 2020. The contribution of high frequency wind-generated surface waves to the Stokes drift. J. Phys. Oceanogr. 1–39.
Longuet-Higgins, M.S., Stewart, R.W., 1962. Radiation stress and mass transport in gravity waves, with application to 'surf beats'. J. Fluid Mech. 13, 481–504.
Marchesiello, P., McWilliams, J.C., Shchepetkin, A., 2001. Open boundary conditions for long-term integration of regional oceanic models. Ocean Model. 3, 1–20.
Mason, E., Molemaker, J., Shchepetkin, A.F., Colas, F., McWilliams, J.C., Sangrà, P., 2010. Procedures for offline grid nesting in regional ocean models. Ocean Model. 35, 1–15.
McWilliams, J.C., Restrepo, J.M., 1999. The wave-driven ocean circulation. J. Phys. Oceanogr. 29, 2523–2540.
McWilliams, J.C., Restrepo, J.M., Lane, E.M., 2004. An asymptotic theory for the interaction of waves and currents in coastal waters. J. Fluid Mech. 511, 135–178.
McWilliams, J.C., Sullivan, P.P., Moeng, C.-H., 1997. Langmuir turbulence in the ocean. J. Fluid Mech. 334, 1–30.
Moghimi, S., Thomson, J., Özkan-Haller, T., Umlauf, L., Zippel, S., 2016. On the modeling of wave-enhanced turbulence nearshore. Ocean Model. 103, 118–132.
Orlanski, I., 1976. A simple boundary condition for unbounded hyperbolic flow. J. Comput. Phys. 21, 251–269.
Phillips, O.M., 1977. The dynamics of the upper ocean. In: Cambridge Monographs on Mechanics and Applied Mathematics, vol. 2, Cambridge University Press.
Qiao, F., Yuan, Y., Yang, Y., Zheng, Q., Xia, C., Ma, J., 2004. Wave-induced mixing in the upper ocean: Distribution and application to a global ocean circulation model. Geophys. Res. Lett. 31, 2–5.
Rascle, N., Ardhuin, F., Terray, E.A., 2006. Drift and mixing under the ocean surface: A coherent one-dimensional description with application to unstratified conditions. J. Geophys. Res. Ocean. 111, 1–16.
Renault, L., Molemaker, M.J., McWilliams, J.C., Shchepetkin, A.F., Lemarié, F., Chelton, D., Illig, S., Hall, A., 2016. Modulation of wind work by oceanic current interaction with the atmosphere. J. Phys. Oceanogr. 46, 1685–1704.
Resio, D.T., Long, C.E., Vincent, C.L., 2004. Equilibrium-range constant in wind-generated wave spectra. J. Geophys. Res. 109, C01018.
Romero, L., 2019. Distribution of surface wave breaking fronts. Geophys. Res. Lett. 46, 10463–10474.
Romero, L., Hypolite, D., McWilliams, J.C., 2020. Submesoscale current effects on surface waves. Ocean Model. 153, 101662.
Romero, L., Melville, W.K., 2010. Airborne observations of fetch-limited waves in the Gulf of Tehuantepec. J. Phys. Oceanogr. 40, 441–465.
Romero, L., Ohlmann, J.C., Pallàs-Sanz, N.M., Pérez-Brunius, P., Maritorena, S., 2019. Coincident observations of dye and drifter relative dispersion over the inner shelf. J. Phys. Oceanogr. 49, 2447–2468.
Romero, L., Siegel, D.A., McWilliams, J.C., Uchiyama, Y., Jones, C., 2016. Characterizing storm water dispersion and dilution from small coastal streams. J. Geophys. Res. Ocean. 121, http://dx.doi.org/10.1002/2015JC011323.
Romero, L., Uchiyama, Y., Ohlmann, J.C., McWilliams, J.C., Siegel, D.A., 2013. Simulations of nearshore particle-pair dispersion in Southern California. J. Phys. Oceanogr. 43, 1862–1879.
Staneva, J., Alari, V., Breivik, J.R., Mogensen, K., 2017. Effects of wave-induced forcing on a circulation model of the North sea. Ocean Dyn. 67, 81–101.
Sullivan, P.P., McWilliams, J.C., Melville, W.K., 2007. Surface gravity wave effects in the oceanic boundary layer: Large-Eddy simulation with vortex force and stochastic breakers. J. Fluid Mech. 593, 405–452.
Sullivan, P.P., Romero, L., McWilliams, J.C., Melville, W.K., 2012. Transient evolution of Langmuir turbulence in ocean boundary layers driven by hurricane winds and waves. J. Phys. Oceanogr. 42, 1959–1980.
Sutherland, P., Melville, W.K., 2015. Field measurements of surface and near-surface turbulence in the presence of breaking waves. J. Phys. Oceanogr. 45, 943–965.
Terray, E.A., Brumley, B., Strong, B., 1999. Measuring waves and currents with an upward-looking ADCP. In: Proceedings of the IEEE Sixth Working Conference on Current Measurement (Cat. No.99CH36331), pp. 66–71.
Terray, E.A., Donelan, M.A., Agrawal, Y.C., Drennan, W.M., Kahma, K.K., Williams, a.J., Hwang, P.a., Kitaigorodskii, S.a., 1996. Estimates of kinetic energy dissipation under breaking waves.
The WAVEWATCH III Development Group [WW3DG], 2016. User Manual and System Documentation of WAVEWATCH III Version 5.16. Tech. Note 329. Technical note, MMAB Contribution, 276, NOAA/NWS/NCEP/MMAB, College Park, MD, USA, 326 pp. Appendices.
Tolman, H.L., Booij, N., 1998. Modeling wind waves using wavenumber-direction spectra and a variable wavenumber grid. Glob. Atmos.Ocean Syst. 6, 295–309.
Tracy, B., Devaliere, E., Hanson, J., Nicolini, T., Tolman, H., 2007. Wind sea and swell delineation for numerical wave modeling. In: 10th International Workshop on Wave Hindcasting and Forecasting Coastal Hazard Symposium, pp. P12.
Uchiyama, Y., McWilliams, J.C., Shchepetkin, A.F., 2010. Wave–current interaction in an oceanic circulation model with a vortex-force formalism: Application to the surf zone. Ocean Model. 34, 16–35.
Umlauf, L., Burchard, H., 2003. A generic length-scale equation for geophysical turbulence models. J. Mar. Res. 61, 235–265.
Webb, A., Fox-Kemper, B., 2015. Impacts of wave spreading and multidirectional waves on estimating Stokes drift. Ocean Model. 96, 49–64.
Weichman, P., Glazman, R., 2000. Passive scalar transport by travelling wave fields. J. Fluid Mech. 420, 147–200.
Wu, L., Staneva, J., Breivik, A., Nurser, A.G., Clementi, E., Madec, G., 2019. Wave effects on coastal upwelling and water level. Ocean Model. 140, 101405.